

Received February 2, 2020, accepted February 27, 2020, date of publication March 3, 2020, date of current version March 16, 2020.

Digital Object Identifier 10.1109/ACCESS.2020.2978147

Fuzzy Gain Scheduled-Sliding Mode Rotational Speed Control of an Oscillating Water Column

FARES M'ZOUGHI^{ID 1}, IZASKUN GARRIDO^{ID 1}, (Senior Member, IEEE),
AITOR J. GARRIDO^{ID 1}, (Senior Member, IEEE), AND MANUEL DE LA SEN^{ID 2}

¹Automatic Control Group (ACG), Department of Automatic Control and Systems Engineering, Faculty of Engineering of Bilbao, Institute of Research and Development of Processes (IIDP), University of the Basque Country (UPV/EHU), 48013 Bilbao, Spain

²Automatic Control Group (ACG), Department of Electricity and Electronics, Faculty of Science and Technology, Institute of Research and Development of Processes (IIDP), University of the Basque Country (UPV/EHU), 48080 Leioa, Spain

Corresponding author: Fares M'zoughi (fares.mzoughi@ehu.eus)

This work was supported in part by the Basque Government, through project under Grant IT1207-19, and in part by the MCIU/MINECO through under Grant RTI2018-094902-B-C21/RTI2018-094902-B-C22 (MCIU/AEI/FEDER, UE).

ABSTRACT The generated power of Oscillating Water Columns (OWC) based on Wells turbines is limited due to the stalling behavior. Therefore, this paper presents the modeling of an OWC and a rotational speed control using a novel Fuzzy Gain Scheduled-Sliding Mode controller (FGS-SMC) for a stalling-free operation. The proposed SMC-rotational speed control will regulate the turbo-generator angular velocity to avoid the stalling behavior and increase the generated power. In an effort to reduce the fluctuations in the generated power, Fuzzy Logic Supervisors (FLS) were designed to adaptively schedule the switching gains of the SMC controller to reduce the chattering and improve its performance. A comparative study has been carried out between the FGS-SMC, the SMC and uncontrolled OWC using irregular waves and real measured waves. Results show the effectiveness of the proposed controls against the uncontrolled case and the superior performance of FGS-SMC over the SMC ensuring power generation improvement.

INDEX TERMS Back-to-back converter, fuzzy gain scheduling (FGS), sliding mode control (SMC), oscillating water column (OWC), power generation, stalling behavior, wave energy, wells turbine.

I. INTRODUCTION

Climate change, air pollution and energy security issues all over the world require a massive and rapid transformation of the world's energy infrastructure toward a green, renewable energy with zero-emissions. This has been confirmed after the release of the United Nations' Intergovernmental Panel on Climate Change's (IPCC) three Special Reports in the current Sixth Assessment Report (AR6) cycle [1]–[3]. Amongst the key finding of the reports were; the desertification, land degradation, GHG fluxes, rising seas, ocean deoxygenation and melting glaciers but the most important statement was in SR15 about the possibility to meet a 1.5°C target. SR15 shows by modelling that, in order to limit global-warming at 1.5°C, global-emissions of CO₂ should dropdown 45% less than 2010 level by 2030, till it reaches 'net zero' by 2050 [1]. The emission cutback by 2030 and the related adjustments and difficulties were the center of

attention in COP24 at Poland in December 2018 to help set roadmaps for Europe and parties of the UNFCCC.

Such roadmaps evoked the role of the oceans as part of the European efforts to implement the Paris Agreement on Climate Change at the Oceans Action Day at COP22 in Marrakesh where the Ocean Energy Forum charted a strategic roadmap to building ocean energy for Europe, this roadmap claims that 10% of Europe's energy needs can be provided by wave and tidal energy by 2050 [4]. It highlights the importance of R&D to accelerate testing and validation of several ocean technologies to reach a commercial maturity and ensure industrial roll-out [4]. Indeed wave and tidal energy industry are likely to contribute the most to the European energy in the near future [5], [6]. But since wave energy is expected to possess a global-potential 30-times greater than from tidal energy it has the uppermost exploitation potential in European seas [6].

The wave energy industry is at an early development stage when compared. And the fact that many Wave Energy Converter (WEC) developers in different countries are at different

The associate editor coordinating the review of this manuscript and approving it for publication was Xiaowei Zhao.

stage of development there's no common ground for the best configuration, best PTO and best control strategies given the difficulties of implementing. The majority of the available industry-scale prototypes in seas possess the simplest control strategies which results in low energy extraction [7]. This signifies that the focal point of research, in following years, have to shift from large-scale wave energy utilization toward the difficulties of developing WECs and customized applications appropriate in favor of niche markets [8]. As stated by the European Marine Energy Centre numerous countries are implicated with projects that focuses on the progress of the WEC industry such as “UK (26 projects), Norway (14), Denmark (9), Spain (9), Ireland (7), Sweden (5), France (4), Finland-Germany-Portugal (2), Greece (1)” [9], [10].

Amongst the WECs projects in Spain, we note NEREIDA wave power plant in Mutriku which was installed by the Basque Energy Agency (EVE) since 2011 and is the first OWC establishment performing like a test-rig for technology developers [11], [12], MARMOK-A-5 as the earliest operating grid-connected floating OWC which was developed in Oceantec in Bilbao and then acquired by IDOM in 2016 [13], WEP+ created in Wedge Global and had 5-years testing in the PLOCAN test-facility of the Canary Islands [7] and LifeDemoWave which is a project testing an unconnected 25kW prototype in the Galician-coast since 2018 [14].

The most employed wave energy system is the Oscillating Water Column (OWC). Many control strategies have been proposed by researchers the last decade to control various aspects of this type of system. Airflow control strategy has been proposed to OWC converters to control the airflow rate through the turbine which should be prevented from exceeding the threshold beyond which severe internal aerodynamic blade stalling reduces the power output. This is achieved by using a throttle valve (in series) or a by-pass valve (in parallel) as suggested by Falcão *et al.* [15]. This strategy have been further implemented using various control approaches such as the PID controllers used by Amundarain *et al.* [16], Fractional order PID (FOPID) by Mishra *et al.* [17] and Optimization algorithms by Mzoughi *et al.* [18], [19]. Another control strategy proposed for this type of WEC is the rotational speed control, first proposed in 1994 [20] and developed by other authors in 1999 [21], is the most commonly employed OWC control scheme. Justino *et al.* proposed a rotational speed control achieved by changing the electric torque through the power conditioning equipment [21]. Then Falcão *et al.* proposed this control to maximize the power while taking into consideration the electrical efficiency dependence on the load factor and of the constraint introduced by electrical rated power as a threshold power level [22]. Later other authors proposed control approaches for this strategy like the ANN-based rotational speed control by Amundarain *et al.* which allows to generate desired reference speed for the back-to-back converter control scheme that governs the DFIG [23]. Also, a Maximum Power Point Tracking (MPPT) based on Wells turbine-based OWC has been proposed by Lekube *et al.* to optimally vary the speed reference considering the

highest power [24]. And recently Mishra *et al.* investigated numerous techniques for the rotational speed control strategy including a Fuzzy MPPT tracking based backstepping control in [25], an MPPT optimization using PSO algorithm in [26] and event-triggered backstepping controller (ET-BSC) and event-triggered sliding mode controller (ET-SMC) in [27].

The research work discussed in this article studies the control of a Wells turbine-based OWC system for wave energy conversion. The main hurdle with this type of PTO systems is the reduced performance of the Wells turbine because of the stalling behavior which limits the power output [28], [29]. The present article holds a dual objective: first, to suggest a control strategy to evade the inevitable power restriction of the stalling phenomenon and, second, to reduce the fluctuations of the generated power by improving the performance of the fixed gain SMC controller and reducing the chattering phenomenon using intelligent design methodologies. Therefore, a novel SMC-based rotational-speed control has been presented to govern the back-to-back converter and help adjust the angular velocity. The Fuzzy Gain Scheduling (FGS) methodology has been proposed to improve the performance of the basic rotational speed control scheme. The concept uses Fuzzy Logic Systems (FLS) as supervisors to adaptively change the gains in real-time.

The rest of the article has been outlined as follows; A description of all the subsystems of the OWC system and mathematical models are given in Section II. Section III explains the proposed sliding mode rotational speed control to evade the stalling phenomenon. To improve its performance and reduce the chattering, the FGS technique has been introduced to tune the gains in real-time. Section IV sets a demonstrative study-case to examine the goodness of the FGS-SMC-based rotational speed control with irregular and real waves. Finally, Section V ends the article with concluding remarks.

II. MODEL STATEMENT

The OWC system under study consists of different parts that have been modeled for numerical implementation and control purposes. This section presents the modeling of all the necessary element of the plant of Figure 1.

A. WAVE MODEL

The wave model can be defined by a regular sine waveform by means of the Airy theory which neglects turbulences, friction-losses and other energy-losses [30]. Figure 1 shows the scheme of a wave, with SWL is the Still-Water-Level, h is the water-depth, H is the wave-height. A is the wave-amplitude and λ is the wavelength [31].

Thus, the surface elevation of the wave model can be formulated as [15]:

$$z(x, t) = A \sin(\omega t - kx\theta) = \frac{H}{2} \sin(\omega t - kx\theta) \quad (1)$$

where the horizontal coordinate x is directed with the direction of wave propagation, θ represents the angle between

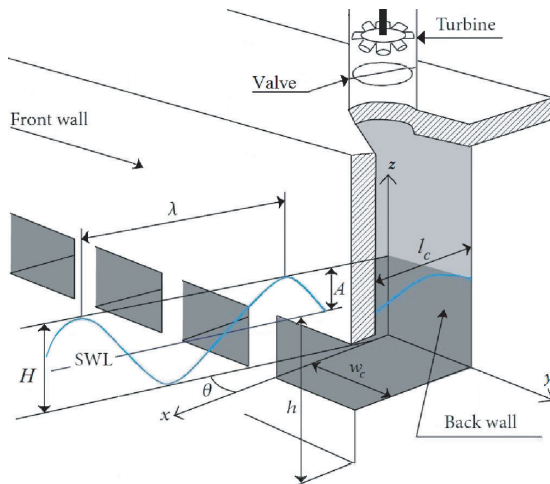


FIGURE 1. Scheme of a sea wave and an Oscillating-Water-Column [32].

the x -axis and the direction of the waves, and k is the wave number defined as:

$$k = 2\pi/\lambda \quad (2)$$

A real irregular wave can be simulated by the superposition of N number of regular waves and described as follows [33]:

$$z(x, t) = \sum_{i=1}^N A_i \sin(\omega_i t - k_i + \theta_i) \quad (3)$$

$$A_i = \sqrt{2S_i \Delta\omega_i} \quad (4)$$

where N is the number of waves, S_i is the Spectral density, A_i is the amplitude of each wave component, λ_i is the wavelength of each component, θ_i is a random phase angle between 0 and 2π , ω_i is the angular frequency and k_i is the wave number of each wave component.

The most accepted theoretical wave spectra include the Bretschneider spectrum for the fully developed waves, and the JONSWAP spectrum for the limited developed waves. The generalized JONSWAP spectrum is defined as [34]:

$$S_i(\omega_i) = (1 - 0.287 \ln(\gamma)) \frac{5\omega_p^4}{16\omega^5} H_s^2 \gamma^\alpha e^{-\frac{5\omega_p^4}{4\omega^4}} \quad (5)$$

where $\alpha = \exp\left(-\frac{(\omega-\omega_p)^2}{2\omega_p^2\sigma^2}\right)$ and $\sigma = \begin{cases} 0.07, & \text{if } \omega \leq \omega_p \\ 0.09, & \text{if } \omega > \omega_p \end{cases}$ and H_s is the significant wave height and ω_p is the peak angular frequency. The peak shape parameter γ is chosen between 1 and 5 depending on the actual wave conditions and locations, for standard JONSWAP spectrum $\gamma = 3.3$ [34].

B. CAPTURE CHAMBER MODEL

The expression of the air volume inside the capture chamber of an OWC is given in [31] as:

$$V(t) = V_c + \frac{w_c H}{k} \sin(kl_c/2) \sin(\omega t) \quad (6)$$

where V_c , w_c and l_c are the capture chamber's volume, inner width and length, respectively.

From (6), the volume flow rate is described as [31]:

$$Q(t) = w_c c H \sin\left(\frac{kl_c}{2}\right) \cos(\omega t) \quad (7)$$

with $c = w_c/k$.

The airflow velocity is described by exploiting (7) and considering the geometry of the air chamber that yields [31]:

$$v_x(t) = \frac{Q(t)}{S} = \frac{8Acw_c}{\pi D^2} \sin\left(\frac{\pi l_c}{cT_w}\right) \cos\left(\frac{2\pi}{T_w}t\right) \quad (8)$$

where D is the duct diameter.

C. WELLS TURBINE MODEL

The turbine Wells turbine is a self rectifying axial flow type [35]. The turbine's model is defined in [36] as:

$$dp = C_a K \left(1/a\right) \left[v_x^2 + (r\omega_r)^2\right] \quad (9)$$

$$K = \rho l b n / 2 \quad (10)$$

$$T_t = r C_t K \left[v_x^2 + (r\omega_r)^2\right] \quad (11)$$

$$\phi = v_x (r\omega_r)^{-1} \quad (12)$$

$$Q = av_x \quad (13)$$

$$\eta_t = T_t \omega_r (dp Q)^{-1} = C_t (C_a \phi)^{-1} \quad (14)$$

with dp is the pressure-drop, C_a and C_t are the power and torque coefficients, ϕ is the flow coefficient, T_t , η_t , K , r are respectively the turbine's torque, performance, constant and mean radius, l , b , n are respectively the blade's chord-length, height and number, ω_r is the rotational speed, a is the cross sectional area and ρ is the air density.

Figures 2 and Figure 3 show the characteristic curves of the Wells turbine under study. Figure 2 is the power coefficient C_a against flow coefficient ϕ while Figure 3 is the torque coefficient C_t against flow coefficient ϕ . These characteristic curves allow computing the turbine torque and generated power.

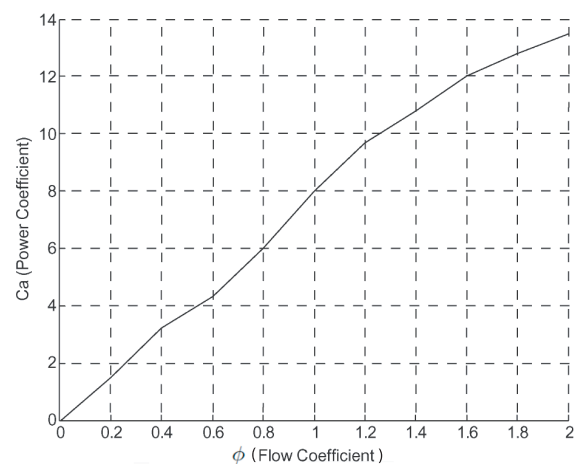


FIGURE 2. Power coefficient against flow coefficient [16].

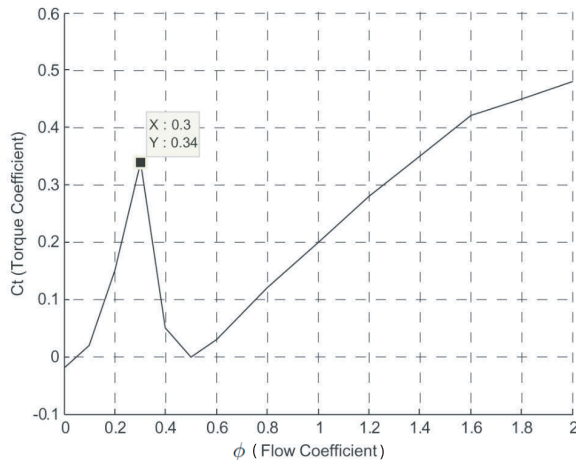


FIGURE 3. Torque coefficient against flow coefficient [16].

D. DOUBLY FED INDUCTION GENERATOR MODEL

The DFIG is modeled with the expressions defined in [37]. The stator and rotor voltages in d - q frame are defined as:

$$\begin{cases} v_{ds} = R_s i_{ds} + \frac{d\psi_{ds}}{dt} - \omega_s \psi_{qs} \\ v_{qs} = R_s i_{qs} + \frac{d\psi_{qs}}{dt} + \omega_s \psi_{ds} \end{cases} \quad (15)$$

$$\begin{cases} v_{dr} = R_r i_{dr} + \frac{d\psi_{dr}}{dt} - \omega_r \psi_{qr} \\ v_{qr} = R_r i_{qr} + \frac{d\psi_{qr}}{dt} + \omega_r \psi_{dr} \end{cases} \quad (16)$$

where R_s and R_r are the stator and rotor resistances, ω_s and ω_r are the stator and rotor angular velocity, i_{ds} and i_{qs} are the d - q stator currents, i_{dr} and i_{qr} are the d - q rotor currents.

The stator and rotor flux linkage described as:

$$\begin{cases} \psi_{ds} = L_{ss} i_{ds} + L_m i_{dr} \\ \psi_{qs} = L_{ss} i_{qs} + L_m i_{qr} \end{cases} \quad (17)$$

$$\begin{cases} \psi_{dr} = L_{rr} i_{dr} + L_m i_{ds} \\ \psi_{qr} = L_{rr} i_{qr} + L_m i_{qs} \end{cases} \quad (18)$$

with L_{ss} , L_{rr} and L_m are the stator, rotor and magnetizing inductances, respectively.

The DFIG's electromagnetic torque expression is given by:

$$T_e = \frac{3}{2} p (\psi_{ds} i_{qs} - \psi_{qs} i_{ds}) \quad (19)$$

with p is the number of pair poles of the DFIG.

The interaction in the turbo-generator is described by:

$$J \frac{d\omega_r}{dt} = T_e - T_t \quad (20)$$

with J is the system's inertia.

E. BACK-TO-BACK CONVERTER MODEL

The back-to-back converter holds a Grid Side Converter (GSC) coupled to the grid and a Rotor Side Converter (RSC) coupled to the rotor-windings [38].

The function of a rotor side converter is providing voltage to the DFIG's rotor-windings. Its purpose is to align the rotor

flux with the stator flux by controlling the rotor currents to produce the desired torque. Thus it allows regulating the voltages and generated power across the stator [39].

The stator active and reactive powers may be written as:

$$P_s = \frac{3}{2} (v_{ds} i_{ds} + v_{qs} i_{qs}) \quad (21)$$

$$Q_s = \frac{3}{2} (v_{qs} i_{ds} - v_{ds} i_{qs}) \quad (22)$$

The grid voltages can be defined as:

$$\begin{cases} v_{dg} = R_g i_{dg} + L_g \frac{di_{dg}}{dt} - \omega_g L_g i_{qg} + u_{dg} \\ v_{qg} = R_g i_{qg} + L_g \frac{di_{qg}}{dt} + \omega_g L_g i_{dg} + u_{qg} \end{cases} \quad (23)$$

where R_g and L_g are the grid coupling resistance and inductance, ω_g is the grid's angular frequency, i_{dg} and i_{qg} are the d - q grid currents and u_{dg} and u_{qg} are the GSC voltages.

The active and reactive powers between the GSC and the grid are defined as:

$$P_g = \frac{3}{2} (v_{dg} i_{dg} + v_{qg} i_{qg}) \quad (24)$$

$$Q_g = \frac{3}{2} (v_{qg} i_{dg} - v_{dg} i_{qg}) \quad (25)$$

The energy saved in the capacitor is described in [40] as:

$$W_{dc} = \int P_{dc} dt = \frac{1}{2} C v_{dc}^2 \quad (26)$$

with C , v_{dc} , W_{dc} and P_{dc} are the DC-link capacitance, voltage, stored energy and power, respectively.

III. CONTROL STATEMENT

The Wells turbine's stalling effect may be evaded by adjusting the flow coefficient [18], [19]. By referring to equation (12), the flow coefficient ϕ may be adjusted by increasing or decreasing the turbo-generator's rotational speed. Hence the proposed control intends to change the rotational speed ω_r to keep up with the airflow velocity v_x in order to maintain the coefficient ϕ below the threshold value. The rotational speed control is accomplished through the control of the AC-DC-AC converter linking the DFIG's rotor to the grid [39], [41]. Figure 4 presents the scheme of the proposed control strategy.

Both sides of the back-to-back converter control different features of the system. The grid-side converter regulates the DC-bus voltage and reactive power, while the rotor-side converter controls the active power and rotational speed. Therefore for the GSC a conventional PI control scheme has been considered which has been proven efficient in many renewable applications. On the other hand for the RSC due to the complexity of the OWC a nonlinear control method with quick convergence properties and a high robustness against parameter variations and external disturbances has been sought, therefore the SMC control has been considered.

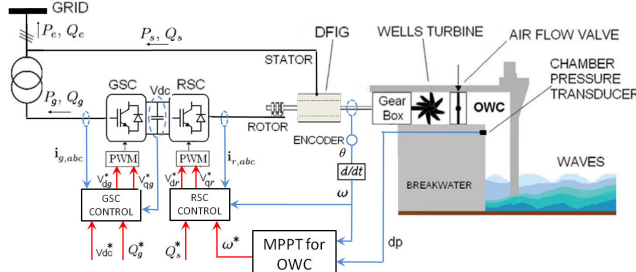


FIGURE 4. Back-to-back converter control for an OWC system.

A. GRID SIDE CONVERTER CONTROL

The vector control by the Voltage Oriented Control (VOC) is employed for the GSC here the d -axis has been aligned with the grid voltage vector [39]. This leads to $v_{dg} = v_g$ and $v_{qg} = 0$. Hence, the grid active and reactive powers become:

$$\begin{cases} P_g = \frac{3}{2} v_{dg} i_{dg} \\ Q_g = -\frac{3}{2} v_{dg} i_{qg} \end{cases} \quad (27)$$

Using the VOC the grid voltages expression become as:

$$\begin{cases} v_{dg} = R_g i_{dg} + L_g \frac{di_{dg}}{dt} + \underbrace{\omega_g L_g i_{qg}}_{\Delta v_{qg}} + u_{dg} \\ 0 = R_g i_{qg} + L_g \frac{di_{qg}}{dt} + \underbrace{\omega_g L_g i_{dg}}_{\Delta v_{dg}} + u_{qg} \end{cases} \quad (28)$$

where Δv_{dg} and Δv_{qg} are the feed forward compensation terms that will be added back to the control signals.

The DC-bus voltage and reactive power regulation is achieved using the control scheme shown in Figure 5. The scheme uses two rows of two PI controllers in series.

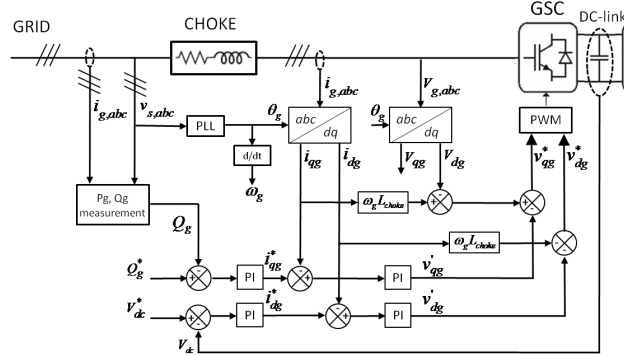


FIGURE 5. Control scheme for the Grid-Side Converter.

The outer loops use PI-controllers and take as reference inputs the grid's reactive power Q_g^* , frequently set to zero, and the reference DC voltage $V_{DC}^* = 800V$ in order to provide the currents i_{dg}^* and i_{qg}^* . These currents are the reference inputs of the inner loops. The inner loops produce the reference voltages v'_{dg} and v'_{qg} that is compensated to attain v_{dg}^* and v_{qg}^* required for the Pulse Width Modulation.

The inner current loops were designed using the pole placement method. By equating the denominator of the closed-loop

transfer function to the general form of a second-order system the PI parameters are found as [42]:

$$\begin{cases} K_{P_{ig}} = 2\xi\omega_n - \frac{R_g}{L_g} \\ T_{I_{ig}} = \frac{2\xi}{\omega_n} - \frac{R_g}{\omega_n^2 L_g} \end{cases} \quad (29)$$

where ξ is the damping coefficient and ω_n is the natural frequency of the desired closed-loop reference model.

The outer loops controllers were designed for the quadrature current, in order to have a null reactive power hence the reference current can be set to zero. For the DC-link voltage using the pole placement, the parameters of the PI controller are found as:

$$\begin{cases} K_{P_{dc}} = 8/3\xi\omega_n C \\ T_{I_{dc}} = 2\xi/\omega_n \end{cases} \quad (30)$$

For design purposes, both parameters are chosen to ensure an overshoot of 5% and since the outer loops generate the current reference for the inner loops hence the inner loop must be faster [42].

B. ROTOR SIDE SLIDING MODE ROTATIONAL SPEED CONTROL

The Sliding Mode Control (SMC) has been successfully used with DFIG to control and improve different aspects for a better performance [43]–[45]. This side of the back-to-back converter is used to control to control the rotational speed and reactive power [46]. To quickly react and adjust the rotational speed when strong wave occurs, a nonlinear controller with quick convergence properties and high robustness against parameter variations due to the nature of the waves has been sought. Therefore the SMC has been considered and further enhanced by FGS. Nevertheless, other control approaches such as the backstepping control present a promising solution for stable power generation [25], [27]. Figure 6 presents the proposed control strategy for the rotor-side converter with SMC.

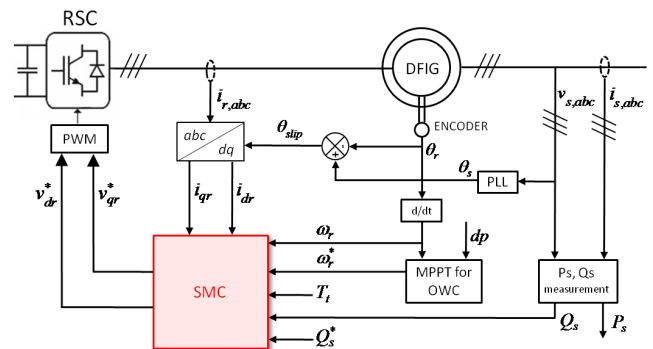


FIGURE 6. Sliding mode rotational speed control scheme for the RSC.

By implementing the Stator Flux Orientation (SFO) vector control for the RSC scheme the d -axis is been aligned with the stator flux vector and by assuming that the flux stable and constant we find that $\varphi_{ds} = \varphi_s$ and $\varphi_{qs} = 0$ [39], [41]. Also,

by assuming the stator resistors are very small to be neglected the stator voltages become:

$$\begin{cases} v_{ds} = 0 \\ v_{qs} = v_s = \omega_s \varphi_s \end{cases} \quad (31)$$

After replacing expressions (17) and (18) in (16) the rotor voltages becomes [46]:

$$\begin{cases} v_{dr} = R_r i_{dr} + \sigma L_r \frac{di_{dr}}{dt} - \omega_r \psi_{qr} \\ v_{qr} = R_r i_{qr} + \sigma L_r \frac{di_{qr}}{dt} + \omega_r \psi_{dr} \end{cases} \quad (32)$$

where $\sigma = 1 - L_m^2/L_s L_r$ is the dispersion coefficient.

Also, the electromagnetic torque equation (19) and reactive power equation (22) become [46]:

$$T_e = -\frac{3}{2} p \frac{L_m}{L_s} \psi_s i_{qr} \quad (33)$$

$$Q_s = \frac{3}{2} v_s \left(\frac{\psi_s}{L_s} - \frac{L_m}{L_s} i_{dr} \right) \quad (34)$$

By replacing equation (33) in expression (20) it yields:

$$\frac{d\omega_r}{dt} = -\frac{p}{J} \left(\frac{3}{2} p \frac{L_m}{L_s} \psi_s i_{qr} + T_t + f \omega_r \right) \quad (35)$$

Looking into equation (34) and equation (35) the rotational speed and reactive power can be governed by i_{dr} and i_{qr} . Therefore, both switching functions e_d and e_q were specified for the synthesis of the sliding mode controller by [46], [47]:

$$\begin{cases} e_d = Q_s^* - Q_s \\ e_q = \frac{d\omega_r^*}{dt} - \frac{d\omega_r}{dt} \end{cases} \quad (36)$$

The switching functions are used to describe the sliding surfaces ($e_d = 0$ and $e_q = 0$) by [47], [48]:

$$\begin{cases} S_d = \dot{e}_d + \lambda_d e_d \\ S_q = \dot{e}_q + \lambda_q e_q \end{cases} \quad (37)$$

where λ_d and λ_q chosen as real positive constants.

The sliding mode controllers have been synthesized to attract the switching functions toward the corresponding sliding-surface when in the transient state [47], [48]. Thus i_{dr} and i_{qr} tend towards their references. Therefore, these switching functions as well as their time-derivatives should meet the next attractive conditions [49]:

$$\begin{cases} \dot{e}_d e_d < 0 \\ \dot{e}_q e_q < 0 \end{cases} \quad (38)$$

Once the sliding surfaces are reached, the invariance conditions of equation (39) have to be met in order to uphold these switching functions at the sliding surfaces [47], [48]:

$$\begin{cases} e_d = 0 \quad \text{and} \quad \dot{e}_d = 0 \\ e_q = 0 \quad \text{and} \quad \dot{e}_q = 0 \end{cases} \quad (39)$$

The d - q reference voltages have to be computed to check the attractive and invariance conditions. Hence, the reference rotor voltages v_{dr}^* and v_{qr}^* has been described by:

$$\begin{cases} v_{dr}^* = v_{dr}^{att} + v_{dr}^{eqv} \\ v_{qr}^* = v_{qr}^{att} + v_{qr}^{eqv} \end{cases} \quad (40)$$

where v_{dr}^{att} and v_{qr}^{att} are the attractive voltages, and v_{dr}^{eqv} and v_{qr}^{eqv} are the equivalent voltages computed from (39).

By substituting the rotor voltages (32) in the invariance condition of equation (39) the equivalent voltages may be defined as [46]:

$$\begin{cases} e_d = 0 \\ \dot{e}_d = 0 \end{cases} \Rightarrow \begin{cases} Q_s = Q_s^* \\ v_{dr}^{eqv} = R_r i_{dr} - \omega_r \psi_{qr} \\ -\frac{2}{3} \frac{L_s L_r}{L_m} \frac{\sigma}{v_s} \dot{Q}_s^* \end{cases} \quad (41)$$

$$\begin{cases} e_q = 0 \\ \dot{e}_q = 0 \end{cases} \Rightarrow \begin{cases} \dot{\omega}_r = \dot{\omega}_r^* \\ v_{qr}^{eqv} = \psi_{qr} + \omega_r \psi_{dr} \\ + \frac{2 L_s R_r}{3 L_m p \psi_s} \left(\frac{J}{p} \dot{\omega}_r^* - f \omega_r^* - T_t \right) \end{cases} \quad (42)$$

The attractive voltages are defined as [46], [49]:

$$\begin{cases} v_{dr}^{att} = K_d \operatorname{sgn}(S_d) \\ v_{qr}^{att} = K_q \operatorname{sgn}(S_q) \end{cases} \quad (43)$$

where K_d and K_q are real and positive constants.

To prove that the controlled system with SMC control law in (40) along the direct component is asymptotically stable, we choose a Lyapunov function candidate [50], [51] as:

$$W_d(t) = \frac{1}{2} S_d(t) \cdot S_d(t) \quad (44)$$

The time derivative of the Lyapunov function (44) is then:

$$\dot{W}_d(t) = S_d(t) \cdot \dot{S}_d(t) = (\ddot{e}_d(t) + \lambda_d \dot{e}_d(t)) \quad (45)$$

By calculating the time derivatives of (36) we obtain:

$$\begin{cases} \dot{e}_d = \dot{Q}_s^* - \frac{3}{2} \frac{V_s L_m}{\sigma L_s L_r} (V_{dr}^* - R_r i_{dr} + \omega_r \psi_{dr}) \\ \ddot{e}_d = \ddot{Q}_s^* - \frac{3}{2} \frac{V_s L_m}{\sigma L_s L_r} (\dot{V}_{dr}^* - R_r \dot{i}_{dr} + \frac{d(\omega_r \psi_{dr})}{dt}) \end{cases} \quad (46)$$

When substituting (41) and (43) in (46) we obtain:

$$\begin{cases} \dot{e}_d = -\frac{3}{2} \frac{V_s L_m}{\sigma L_s L_r} (K_d \operatorname{sgn}(S_d)) \\ \ddot{e}_d = -\frac{3}{2} \frac{V_s L_m}{\sigma L_s L_r} (K_d \frac{d}{dt} (\operatorname{sgn}(S_d))) \end{cases} \quad (47)$$

Hence equation (45) can be rewritten as:

$$\begin{aligned} \dot{W} &= S_d \cdot \left[\frac{-3}{2} \frac{V_s L_m K_d}{\sigma L_s L_r} \left(\frac{d(\operatorname{sgn}(S_d))}{dt} + \lambda_d \operatorname{sgn}(S_d) \right) \right] \\ &= -\frac{3}{2} \frac{V_s L_m}{\sigma L_s L_r} K_d \left(\frac{d}{dt} |S_d| + \lambda_d |S_d| \right) \end{aligned}$$

$$\begin{aligned}
&= -\frac{3}{2} \frac{V_s L_m}{\sigma L_s L_r} K_d \left(\frac{S_d + \lambda_d}{|S_d|} \right) \\
&= -\frac{3}{2} \frac{V_s L_m}{\sigma L_s L_r} K_d \left(\frac{S_d + \lambda_d}{|S_d|} \right) < 0, \quad (\lambda_d > |S_d|) \quad (48)
\end{aligned}$$

Similarly to the d -axis, the following Lyapunov function has been chosen for the quadrature component:

$$W_q(t) = \frac{1}{2} S_q(t) \cdot S_q(t) \quad (49)$$

The time derivative of the Lyapunov function (49) is then:

$$\dot{W}_q(t) = S_q(t) \cdot \dot{S}_q(t) = (\ddot{e}_q(t) + \lambda_d \dot{e}_q(t)) \quad (50)$$

By calculating the time derivatives of (36) we obtain:

$$\begin{cases} \dot{e}_q = \ddot{\omega}_r^* - \frac{p}{J} \left[\frac{3p\psi_s L_m}{2R_r L_s} (\dot{V}_{qr}^{eqv} + \dot{V}_{qr}^{att} - \ddot{\psi}_{dr} \right. \\ \quad \left. - \frac{d}{dt}(\omega_r \psi_{dr}) \right] + \dot{T}_t + f \dot{\omega}_r^* \\ \ddot{e}_q = \frac{d\ddot{\omega}_r^*}{dt} - \frac{p}{J} \left[\frac{3p\psi_s L_m}{2R_r L_s} (\dot{V}_{qr}^{eqv} + \ddot{V}_{qr}^{att} \right. \\ \quad \left. - \frac{d\psi_{dr}}{dt} - \frac{d^2}{dt^2}(\omega_r \psi_{dr}) \right] + \dot{T}_t + f \dot{\omega}_r^* \end{cases} \quad (51)$$

By substituting (42), (43) and (51) in (50) we get:

$$\begin{aligned} \dot{W}_q &= S_q \cdot \left[\frac{-3}{2} \frac{p^2 \psi_s L_m K_q}{JR_r L_s} \left(\frac{d^2(sgn(S_q))}{dt^2} + \lambda_q \frac{d(sgn(S_q))}{dt} \right) \right] \\ &= -\frac{3}{2} \frac{p^2 \psi_s L_m K_q}{JR_r L_s} \left(\frac{S_q + \lambda_q}{|S_q|} \right) \\ &= -\frac{3}{2} \frac{p^2 \psi_s L_m K_q}{JR_r L_s} \left(\frac{S_q + \lambda_q}{|S_q|} \right) < 0, \quad (\lambda_q > |S_q|) \quad (52) \end{aligned}$$

From equation (48) and (52) it can be stated that under the conditions $\lambda_d > |S_d|$ and $\lambda_q > |S_q|$, that $\dot{W}_d(t)$ and $\dot{W}_q(t)$ are negative definite functions. Also, $W_d(t)$ and $W_q(t)$ are positive definite functions, and, when $S_d(t)$ and $S_q(t)$ tend to infinity, $W_d(t)$ and $W_q(t)$ tend to infinity. Consequently, it can be concluded that the equilibrium at the origin $S_d(t) = 0$ and $S_q(t) = 0$ are globally asymptotically stable by means of the stability theory of Lyapunov.

The reference rotational speed ω_r will be generated thanks to a Maximum Power Point Tracking (MPPT) algorithm of a Wells turbine-based OWC. The designed OWC-based MPPT integrates the characteristic curve of Figure 3 in order to evade the stalling behavior [18]. Hence according to the incoming waves, the OWC-based MPPT will provide the optimal rotational speed reference for every wave amplitude as illustrates in Figure 7.

To confirm the evasion of the stalling phenomenon, analogous simulations have been carried out to monitor the changes of the flow coefficient versus the rotational speed. The obtained rotational speeds presented in Figure 8 indicate that the optimal speeds correspond to the ones where the flow coefficients are exactly below the threshold value 0.3 this validates the maximum extracted turbine torque in Figure 8.

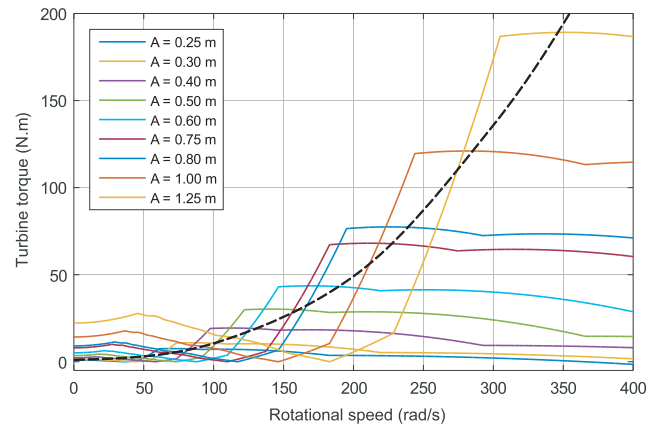


FIGURE 7. Extractable torque against rotational speed for different wave amplitudes [18].

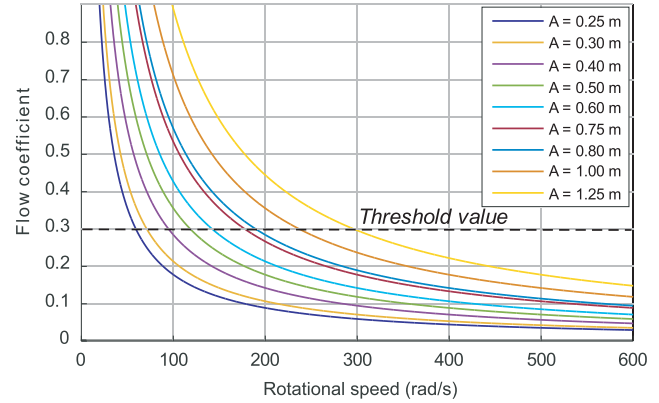


FIGURE 8. Flow coefficient against rotational speed for different wave amplitudes [18].

C. FUZZY GAIN SCHEDULING OF SLIDING MODE ROTATIONAL SPEED CONTROL

Although SMC controllers are robust against uncertainties and structural changes of the system, their performance may be hindered with the chattering phenomenon which occurs when the system state reaches the sliding phase and a high frequency chattering behavior starts forming around the sliding surfaces [52]–[54]. This is due to the fact that the control laws of equation (43) contain the discontinuous *sign* function. Moreover the intensity of this chattering is relative to the control gains K_d and K_q of the *sign* functions. In this context, a design methodology has been proposed and used to enhance the performance of fixed-gain SMC controller. The concept uses the fuzzy gain scheduling approach to adaptively adjust the gains in real-time. Furthermore, the discontinuous *sign* function has been replaced by the continuous *sat* function.

The idea of Fuzzy Gain Scheduling was first introduced by Zhen-Yu Zhao et al. in 1993 [55] for PID controller. Ever since, several industries adopted this tuning technique like renewable energy applications [56]–[58]. The concept of Fuzzy Gain Scheduling has also been introduced and used for applications with Backstepping control [59], [60] and Sliding Mode Control [61]–[63].

The aim is to tune the gains of the proposed rotational speed sliding mode controller λ_d , λ_q , K_d and K_q using a

Fuzzy Logic Supervisor (FLS) based on fuzzy rules and reasoning. Thus the gains will not be constant values; instead, they change depending on the state's changes. This is due to the fact that if the state trajectories drift away of the sliding surfaces and with a high speed, an increase in the control gains is needed to decrease the chattering. But if the state trajectories reach the sliding surfaces with a high speed then a decrease in the gains is required to decrease the chattering [61]. The aforementioned analysis shows that the gains K_d and K_q can be chosen from the sliding surfaces and their time derivatives. Since the sliding surfaces S_d and S_q depend on the tracking errors and the control gains λ_d and λ_q then these gains could be chosen using FLS as well to help converge the states of the system to the sliding surfaces smoothly and faster.

The suggested Fuzzy Gain Scheduled-Sliding Mode rotational speed control scheme for an OWC system is illustrated in Figure 9. Two fuzzy supervisors **FLS1** and **FLS2** were used to tune the gains λ_d and λ_q in real-time. The input to the supervisors are the reactive power and rotational speed errors and their derivatives. The obtained gains serve as the inputs to compute the sliding surfaces S_d and S_q . Another two fuzzy supervisors **FLS3** and **FLS4** were used to tune the gains K_d and K_q in real-time. The input to **FLS3** and **FLS4** are the sliding surfaces S_d and S_q and their derivatives.

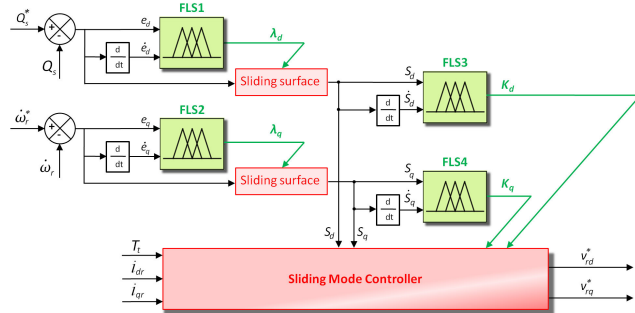


FIGURE 9. Fuzzy gain scheduled sliding mode rotational speed control scheme for OWC.

All four FLS uses a fuzzy inference system with two inputs and one output gain as shown in Figure 9. The controllers gains λ_d , λ_q , K_d and K_q will supposedly be in the pre-defined intervals $[\lambda_d^{\min}, \lambda_d^{\max}]$, $[\lambda_q^{\min}, \lambda_q^{\max}]$, $[K_d^{\min}, K_d^{\max}]$ and $[K_q^{\min}, K_q^{\max}]$, respectively. These intervals were determined using the error-trail method on the SMC controller. Numerous simulations were carried out to determine the max and min values of the control variables by respecting the aforementioned invariance, attractive and asymptotical conditions.

To calculate the SMC controller parameters the well known normalization method has been used which is given in [55] as follows:

$$Y' = (Y - Y^{\min}) / (Y^{\max} - Y^{\min}) \quad (53)$$

where Y is λ_d , λ_q , K_d or K_q and Y' is the fuzzy output acquired from the fuzzy rules that are described of the type IF-THEN as:

$$\text{if } (X \text{ is } A_i \text{ and } \dot{X} \text{ is } B_i) \text{ then } (Y' \text{ is } C_i) \quad (54)$$

where A_i , B_i and C_i are the fuzzy sets with $i = 1, 2, \dots, m$, X is e_d , e_q , S_d or S_q and Y' is the fuzzy output λ'_d , λ'_q , K'_d or K'_q .

The membership functions of the inputs e_j and \dot{e}_j of the fuzzy supervisors **FLS1** and **FLS2** are defined by the fuzzy sets A_i and B_i that are described with the membership functions of Figure 10. On the other hand the membership functions of the inputs S_j and \dot{S}_j of the fuzzy supervisors **FLS3** and **FLS4** are defined by the fuzzy sets A_i and B_i that are described with the membership functions of Figure 11 where $i = 1, 2, \dots, m$ and $j \in \{d, q\}$.

The membership functions employed for the input variables were the triangular and trapezoidal types. The linguistic levels are Negative-Big (NB), Negative (N), Zero (Z), Positive (P), and Positive-Big (PB).

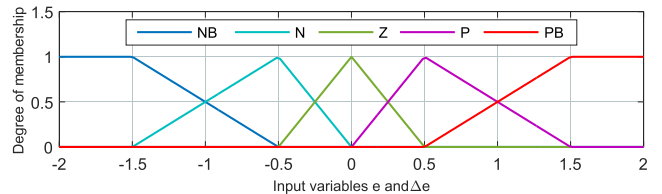


FIGURE 10. Membership functions for inputs e_j and \dot{e}_j in **FLS1** and **FLS2**.

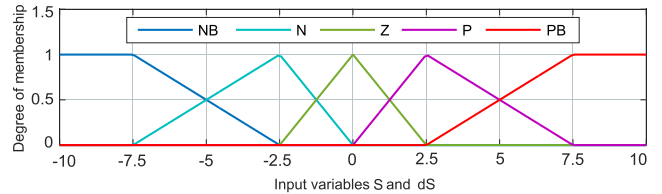


FIGURE 11. Membership functions for inputs S_j and \dot{S}_j in **FLS3** and **FLS4**.

The membership functions for the output variables λ'_d , λ'_q , K'_d and K'_q are described with the fuzzy set C_i , which is described with the functions of Figure 12.

The membership functions employed for the output variables were the triangular and trapezoidal types as well and since the gains λ_d , λ_q , K_d and K_q should be positive the linguistic levels are Zero (Z), Positive-Small (PS), Positive-Medium (PM), Positive (P), and Positive-Big (PB).

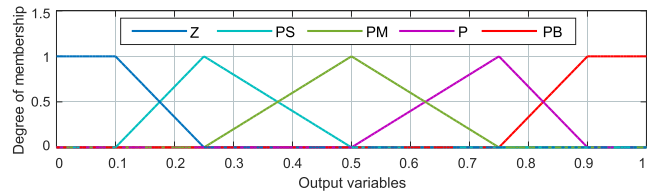


FIGURE 12. Membership functions for outputs in **FLS1** to **FLS4**.

Hence the grade of the membership functions μ_{A_i} and μ_{B_i} for **FLS1** and **FLS2** inputs are:

$$\left\{ \begin{array}{l} \mu_{NB}(X) = \begin{cases} 1 & \text{if } X \leq -\frac{3}{2} \\ (-\frac{1}{2} - X) & \text{if } X \in (-\frac{3}{2}, -\frac{1}{2}) \\ 0 & \text{if } X \geq -\frac{1}{2} \end{cases} \\ \mu_N(X) = \begin{cases} 0 & \text{if } X \leq -\frac{3}{4} \\ (-\frac{X}{2} - \frac{3}{4}) & \text{if } X \in (-\frac{3}{4}, -\frac{1}{2}) \\ -2X & \text{if } X \in (-\frac{1}{2}, 0) \\ 0 & \text{if } X \geq 0 \end{cases} \\ \mu_Z(X) = \begin{cases} 0 & \text{if } X \leq -\frac{1}{2} \\ (2X+1) & \text{if } X \in (-\frac{1}{2}, 0] \\ (1-2X) & \text{if } X \in (0, \frac{1}{2}) \\ 0 & \text{if } X \geq \frac{1}{2} \end{cases} \\ \mu_P(X) = \begin{cases} 0 & \text{if } X \leq 0 \\ 2X & \text{if } X \in (0, \frac{1}{2}] \\ (\frac{3}{2} - X) & \text{if } X \in (\frac{1}{2}, \frac{3}{2}) \\ 0 & \text{if } X \geq \frac{3}{2} \end{cases} \\ \mu_{PB}(X) = \begin{cases} 0 & \text{if } X \leq \frac{1}{2} \\ (X - \frac{1}{2}) & \text{if } X \in (\frac{1}{2}, \frac{3}{2}) \\ 1 & \text{if } X \geq \frac{3}{2} \end{cases} \end{array} \right. \quad (55)$$

where X is the inputs e_d , e_q , \dot{e}_d or \dot{e}_q .

And the grade of the membership functions μ_{A_i} and μ_{B_i} for **FLS3** and **FLS4** inputs are defined as:

$$\left\{ \begin{array}{l} \mu_{NB}(X) = \begin{cases} 1 & \text{if } X \leq -\frac{15}{2} \\ (-\frac{1}{2} - X_5) & \text{if } X \in (-\frac{15}{2}, -\frac{5}{2}) \\ 0 & \text{if } X \geq -\frac{5}{2} \end{cases} \\ \mu_N(X) = \begin{cases} 0 & \text{if } X \leq -\frac{15}{2} \\ (\frac{2X_5 + 3}{2}) & \text{if } X \in (-\frac{15}{2}, -\frac{5}{2}) \\ (\frac{2X_5}{2}) & \text{if } X \in (-\frac{5}{2}, 0) \\ 0 & \text{if } X \geq 0 \end{cases} \\ \mu_Z(X) = \begin{cases} 0 & \text{if } X \leq -\frac{5}{2} \\ (\frac{2X_5 + 1}{2}) & \text{if } X \in (-\frac{5}{2}, 0] \\ (\frac{1-2X_5}{2}) & \text{if } X \in (0, \frac{5}{2}) \\ 0 & \text{if } X \geq \frac{5}{2} \end{cases} \\ \mu_P(X) = \begin{cases} 0 & \text{if } X \leq 0 \\ 2X_5 & \text{if } X \in (0, \frac{5}{2}] \\ (\frac{3}{2} - X_5) & \text{if } X \in (\frac{5}{2}, \frac{15}{2}) \\ 0 & \text{if } X \geq \frac{15}{2} \end{cases} \\ \mu_{PB}(X) = \begin{cases} 0 & \text{if } X \leq \frac{5}{2} \\ (\frac{2X_5 - 1}{2}) & \text{if } X \in (\frac{5}{2}, \frac{15}{2}) \\ 1 & \text{if } X \geq \frac{15}{2} \end{cases} \end{array} \right. \quad (56)$$

where X is the inputs S_d , S_q , \dot{S}_d or \dot{S}_q .

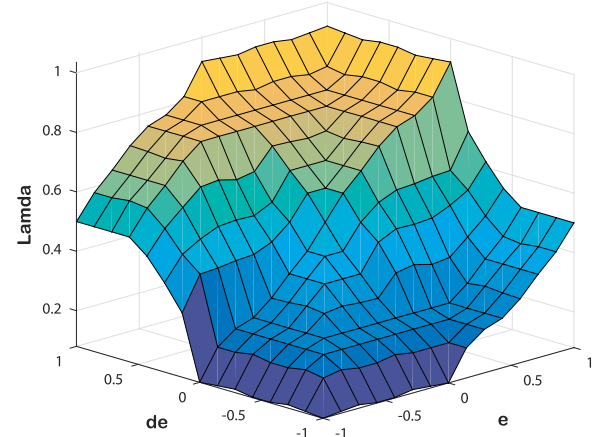


FIGURE 13. Fuzzy surfaces for λ'_d and λ'_q gains.

And the grade of the membership function μ_{C_i} for all supervisors **FLS1** to **FLS4** is defined as:

$$\left\{ \begin{array}{l} \mu_{NB}(X) = \begin{cases} 1 & \text{if } X \leq -\frac{3}{4} \\ (-4X-2) & \text{if } X \in (-\frac{3}{4}, -\frac{1}{2}) \\ 0 & \text{if } X \geq -\frac{1}{2} \end{cases} \\ \mu_N(X) = \begin{cases} 0 & \text{if } X \leq -\frac{3}{4} \\ (4X+3) & \text{if } X \in (-\frac{3}{4}, -\frac{1}{2}) \\ -2X & \text{if } X \in (-\frac{1}{2}, 0) \\ 0 & \text{if } X \geq 0 \end{cases} \\ \mu_Z(X) = \begin{cases} 0 & \text{if } X \leq -\frac{1}{2} \\ (2X+1) & \text{if } X \in (-\frac{1}{2}, 0] \\ (1-2X) & \text{if } X \in (0, \frac{1}{2}) \\ 0 & \text{if } X \geq \frac{1}{2} \end{cases} \\ \mu_P(X) = \begin{cases} 0 & \text{if } X \leq 0 \\ 2X & \text{if } X \in (0, \frac{1}{2}] \\ (3-4X) & \text{if } X \in (\frac{1}{2}, \frac{3}{4}) \\ 0 & \text{if } X \geq \frac{3}{4} \end{cases} \\ \mu_{PB}(X) = \begin{cases} 0 & \text{if } X \leq \frac{1}{2} \\ (4X-2) & \text{if } X \in (\frac{1}{2}, \frac{3}{4}) \\ 1 & \text{if } X \geq \frac{3}{4} \end{cases} \end{array} \right. \quad (57)$$

where X is the outputs λ'_d , λ'_q , K'_d or K'_q .

Two sets of 25-rules were considered for equation (54) and are detailed in Tables 1 and 2. These fuzzy rules were chosen to change the gains depending on the state's evolution, since, if the state trajectories drift away from the sliding surfaces and with a high speed, then an increase in the control gains is needed to decrease the chattering. In contrast, if the state trajectories reach the sliding surfaces with a high speed, then a decrease in the gains is required to decrease the chattering [61]–[63].

The truth value of the i^{th} rule from (54) is found from the product of the truth values of μ_{A_i} and μ_{B_i} as:

$$\mu_i = \mu_{A_i}(e(t)) \cdot \mu_{B_i}(\dot{e}(t)) \quad (58)$$

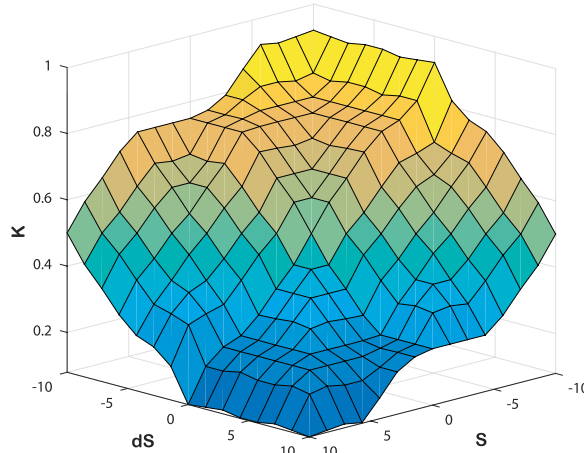


FIGURE 14. Fuzzy surfaces for K'_d and K'_q gains.

TABLE 1. Fuzzy tuning rules for λ'_d and λ'_q .

λ'_j		e_j				
		NB	N	Z	P	PB
e_j	NB	Z	Z	Z	PS	PM
	N	Z	PS	PS	PS	PM
	Z	Z	PS	PM	P	PB
	P	PM	P	P	P	PB
	PB	PM	P	PB	PB	PB

The membership functions illustrated in Figure 12 should always verify the following relation:

$$\sum_{i=1}^m \mu_i = 1 \quad (59)$$

Therefore the defuzzification scheme may be described by:

$$X = \sum_{i=1}^m \mu_i \cdot \mu_{C_i} \quad (60)$$

where X is the output λ'_d , λ'_q , K'_d or K'_q .

The obtained fuzzy surfaces for λ'_d and λ'_q gains are presented with a 3D-plot in Figure 13 and the fuzzy surfaces for K'_d and K'_q are presented with a 3D-plot in Figure 14.

TABLE 2. Fuzzy tuning rules for K'_d and K'_q .

K'_j	S_j					
	NB	N	Z	P	PB	
S_j	NB	PB	PB	P	P	PM
	N	PB	P	P	PM	PS
	Z	PB	P	PM	PS	Z
	P	P	PM	PS	PS	Z
	PB	PM	PS	PS	Z	Z

TABLE 3. OWC system parameters of NEREIDA wave power plant.

JONSWAP	Capture chamber	Wells Turbine
$H_m0=2.44\text{ m}$	$w_c=4.5\text{ m}$	$n=5$
$T_p=10\text{ s}$	$l_c=4.3\text{ m}$	$b=0.21\text{ m}$
$\gamma=3.3$	$\rho_a=1.19\text{ kg/m}^3$	$l=0.165\text{ m}$
	$\rho_w=1029\text{ kg/m}^3$	$r=0.375\text{ m}$
		$a=0.4417\text{ m}^2$
DFIG Generator	Converter	
$R_s=0.5968\Omega$	$P_{rated}=18.45\text{ kW}$	$V_{dc}=800V$
$R_r=0.6258\Omega$	$V_{s rated}=400V$	$C=1200\mu F$
$L_{ss}=0.3495\text{ mH}$	$f_{rated}=50\text{ Hz}$	$R_g=0.0087\Omega$
$L_{rr}=0.324\text{ H}$	$p=2$	$L_g=0.028\text{ H}$
$L_m=0.324\text{ H}$		

TABLE 4. Grid-side converter's PI controllers parameters.

Grid current controllers	DC Voltage controller
$K_{P_{ig}}=19.68$	$K_{P_{dc}}=0.32$
$K_{I_{ig}}=5.26$	$K_{I_{dc}}=5$

The Max-Min fuzzy inference system is used to obtain the crisp outputs which are computed with the center of gravity defuzzification method as:

$$Y = Y^{\min} + (Y^{\max} - Y^{\min}) Y' \quad (61)$$

where Y is λ_d , λ_q , K_d or K_q .

IV. RESULTS AND DISCUSSION

In this part the simulations and tests performed to assess the performance of the proposed rotational speed slid-

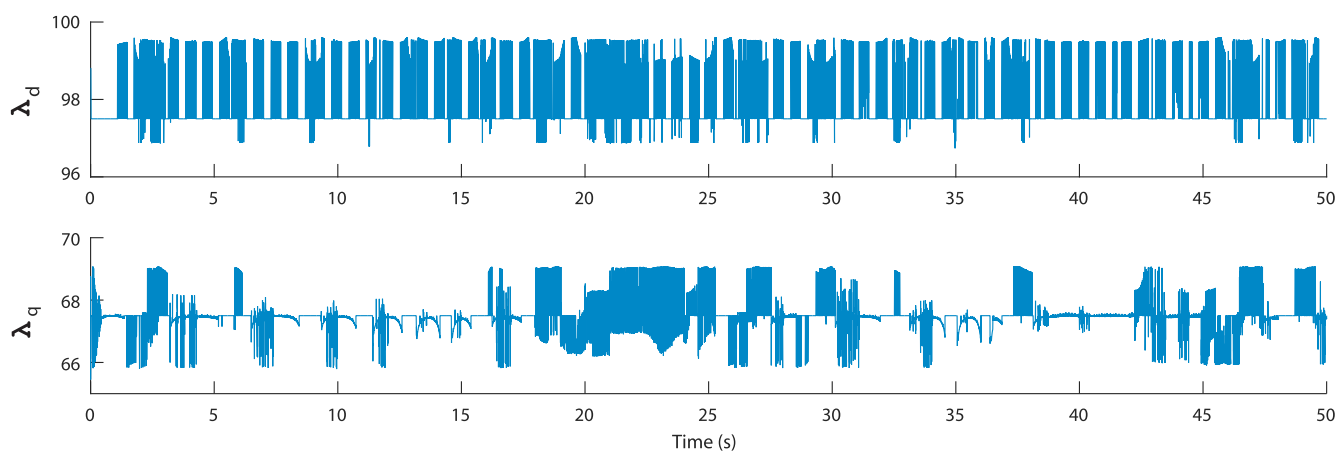


FIGURE 15. Time histories of control gains λ_d and λ_q .

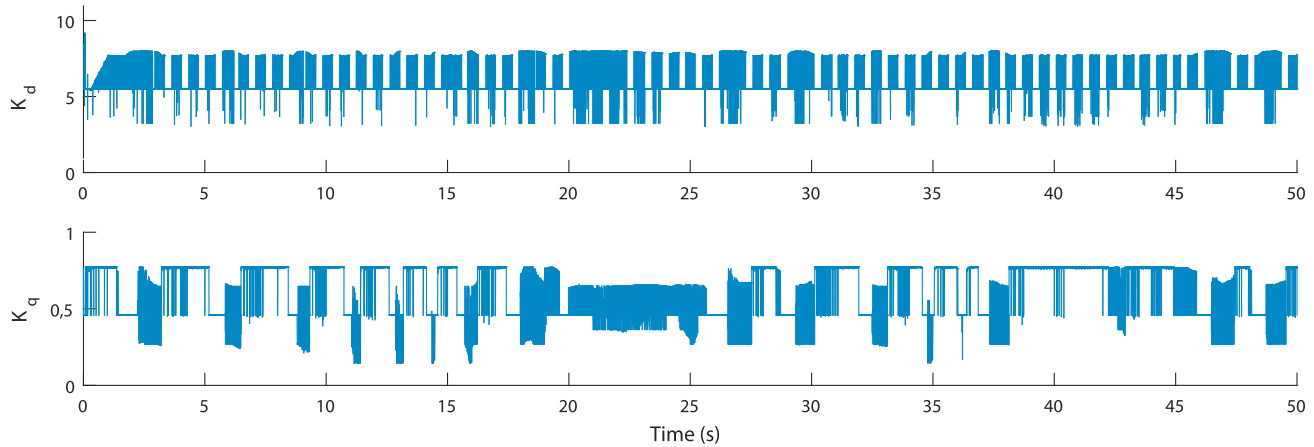


FIGURE 16. Time histories of control gains K_d and K_q .

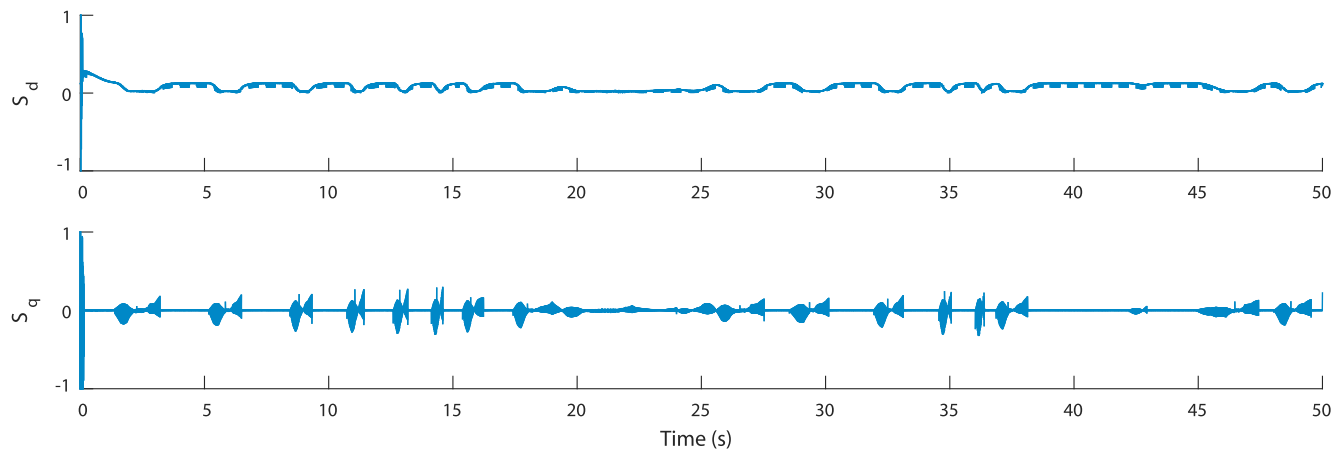


FIGURE 17. Time histories of the sliding variables S_d and S_q using SMC.

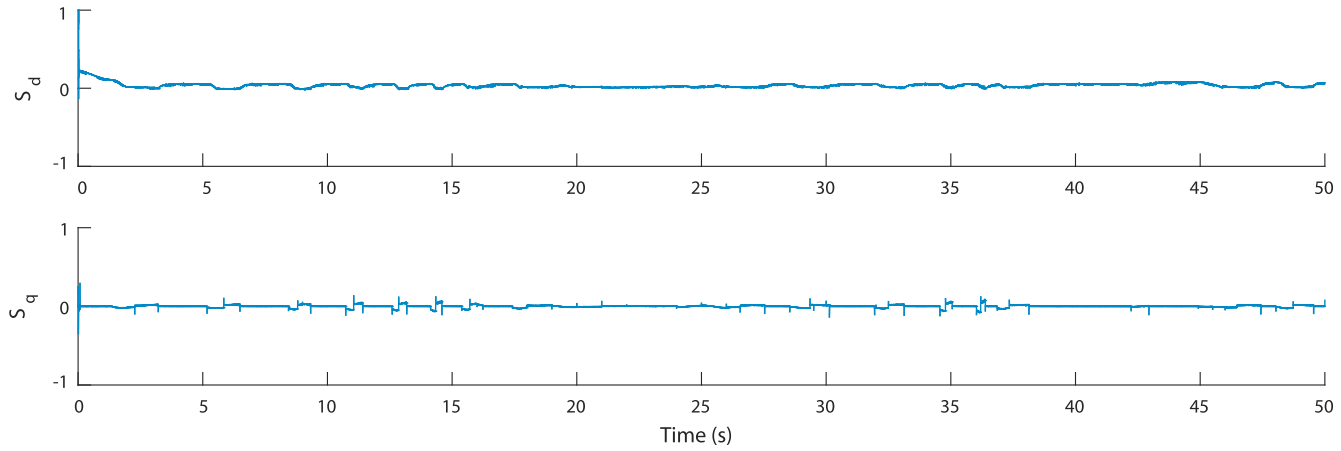


FIGURE 18. Time histories of the sliding variables S_d and S_q using FGS-SMC.

ing mode control with fixed gains and with Fuzzy Gain Scheduling are presented and discussed. To evaluate the performance of the proposed control control methodologies, it has been implemented with a complete wave-to-wire model of the OWC wave power plant on Matlab/Simulink

and a comparison with the uncontrolled case has been performed.

To configure the wave-to-wire OWC model, the parameters taken from real measurements at the NEREIDA facility were used which are listed in Table 3.

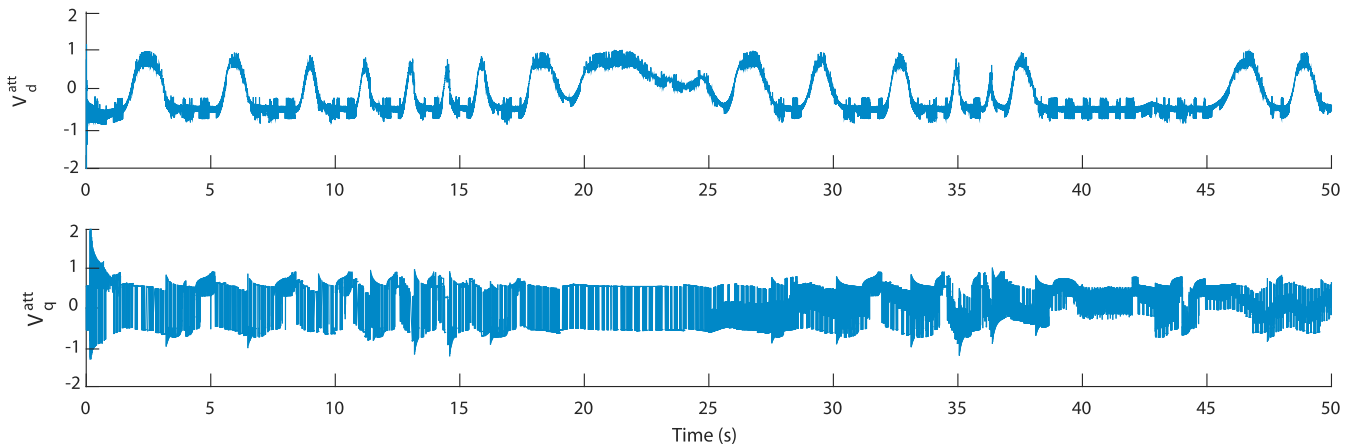


FIGURE 19. Switching detail of the generated attractive control voltages using SMC.

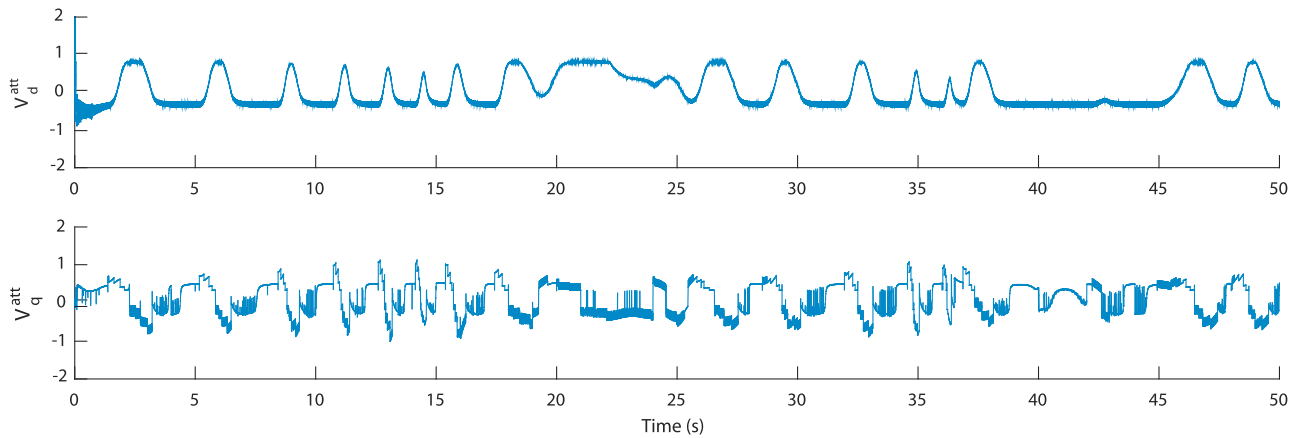


FIGURE 20. Switching detail of the generated attractive control voltages using FGS-SMC.

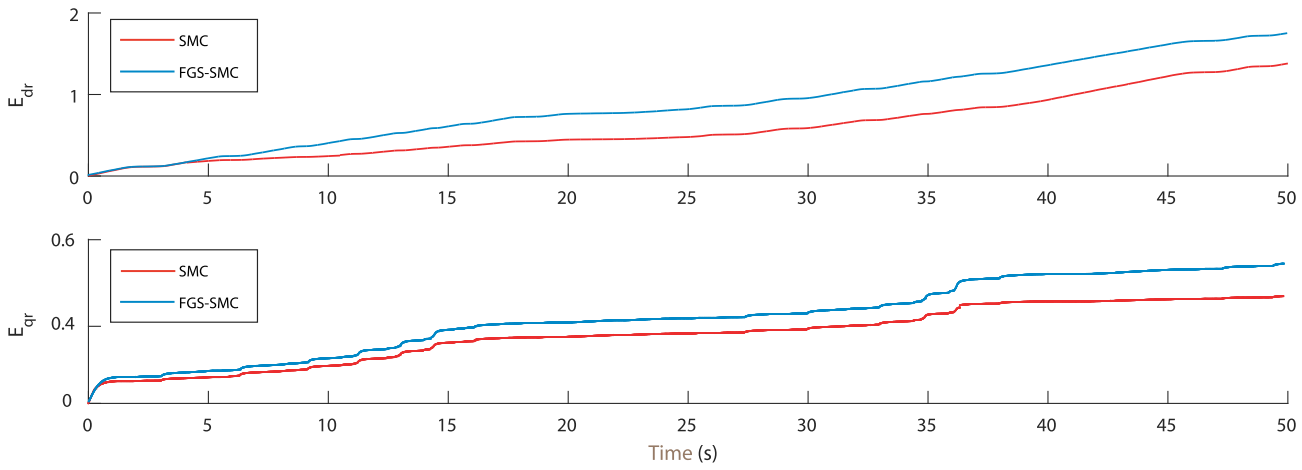


FIGURE 21. Control efforts of SMC and FGS-SMC controllers in both d and q axes.

The implemented PI controllers were set up using the obtained gains in Table 4.

A. CASE STUDY USING IRREGULAR WAVES

To evaluate the power generation enhancement of the proposed control scheme, a study case considering a JONSWAP irregular wave has been carried out. The wave parameters

are representative sea state of Mutriku which are indicated in Table 3.

The study compares the uncontrolled OWC to the Sliding Mode rotational speed control (SMC) and the Fuzzy Gain-Scheduled Sliding Mode rotational speed control (FGS-SMC). In this sense, Figure 15 and Figure 16 show the histories of the scheduled gains of the proposed FGS-SMC.

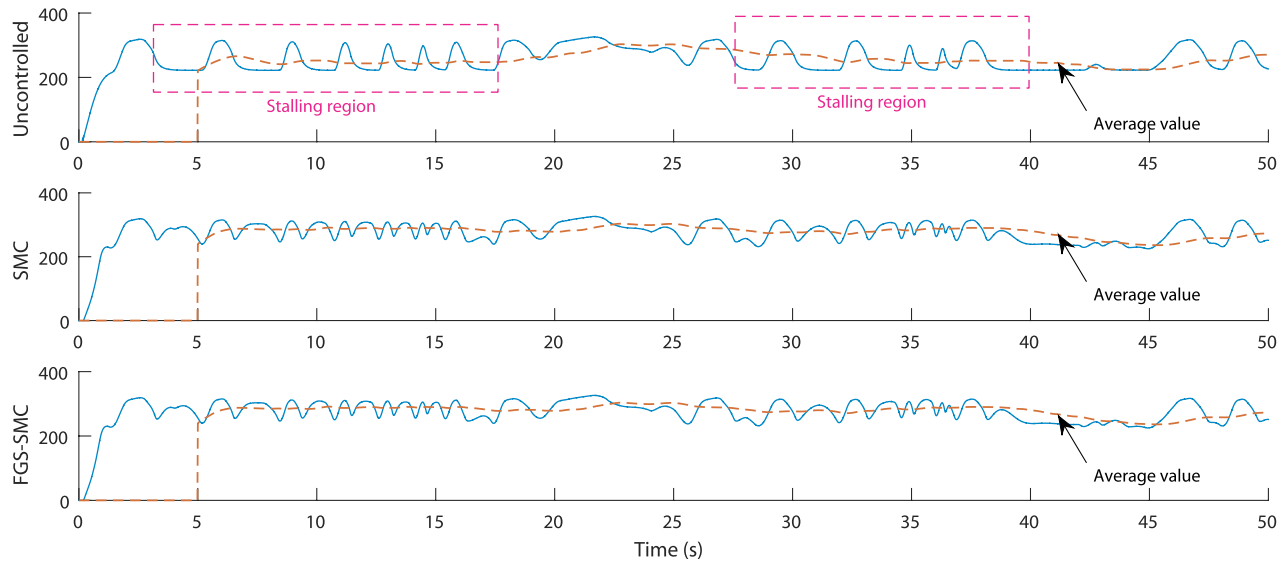


FIGURE 22. Rotational speeds with SMC and FGS-SMC rotational speed control.

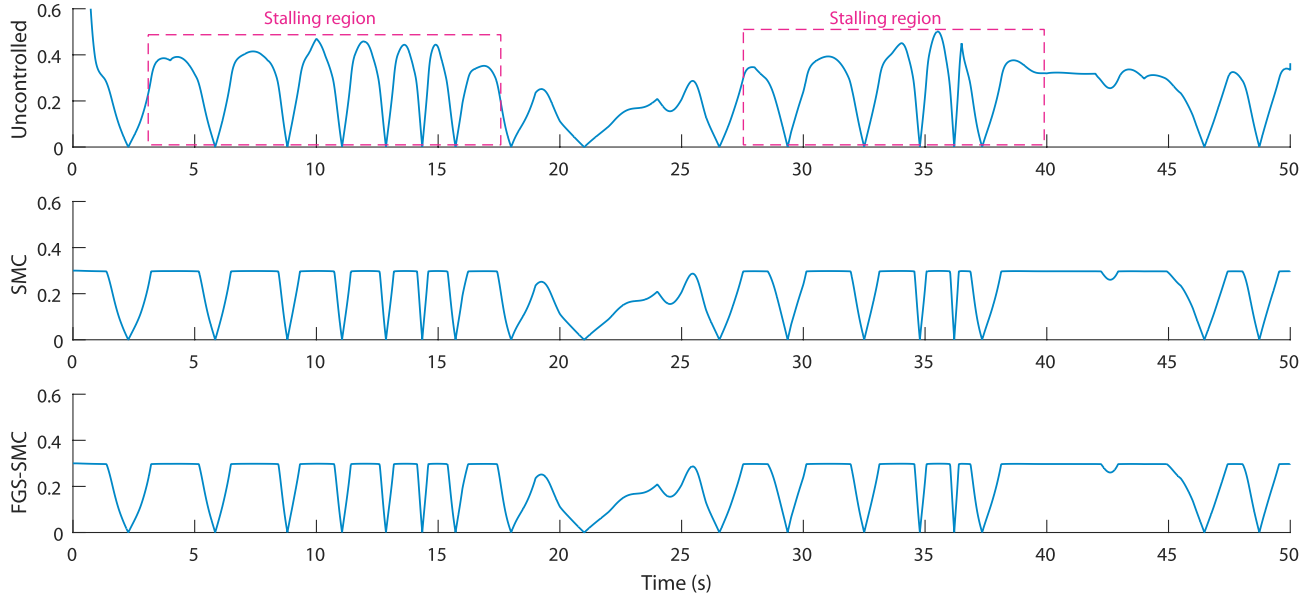


FIGURE 23. Flow coefficients with SMC and FGS-SMC rotational speed control.

Thanks to the adopted fuzzy supervisors **FLS1** to **FLS4** the gains are adaptively scheduled in contrast to conventional SMC.

The sliding variables shown in Figure 17 and Figure 18, slide to zero and are held close to it despite some oscillations in relation to the oscillation of the input waves. Nevertheless, it can be noticed in the sliding variables of the traditional SMC that some chattering occurs at every oscillation of the waves, however, these fluctuations are greatly reduced with the FGS-SMC.

The effect of the adaptive control gains against the fixed-gains may be observed in the generated attractive control voltages v_{dr}^{att} and v_{qr}^{att} which are shown

in Figure 19 and Figure 20. The voltages obtained using SMC suffers from the chattering phenomenon whereas it is greatly reduced when using the FGS-SMC.

To evaluate the performance of the controller the control effort, also known as control energy, has been computed for both SMC and FGS-SMC controllers for comparison. This performance index, defined as the integral of the squared control signal, is shown in Figure 21 where it can be noticed that in the case of the FGS-SMC controller an increase of 19.33% for the direct control and 15.53% for the quadrature control has occurred compared to the SMC controller. This is due to the energy change introduced by the fuzzy gain scheduling to reduce the chattering phenomenon.

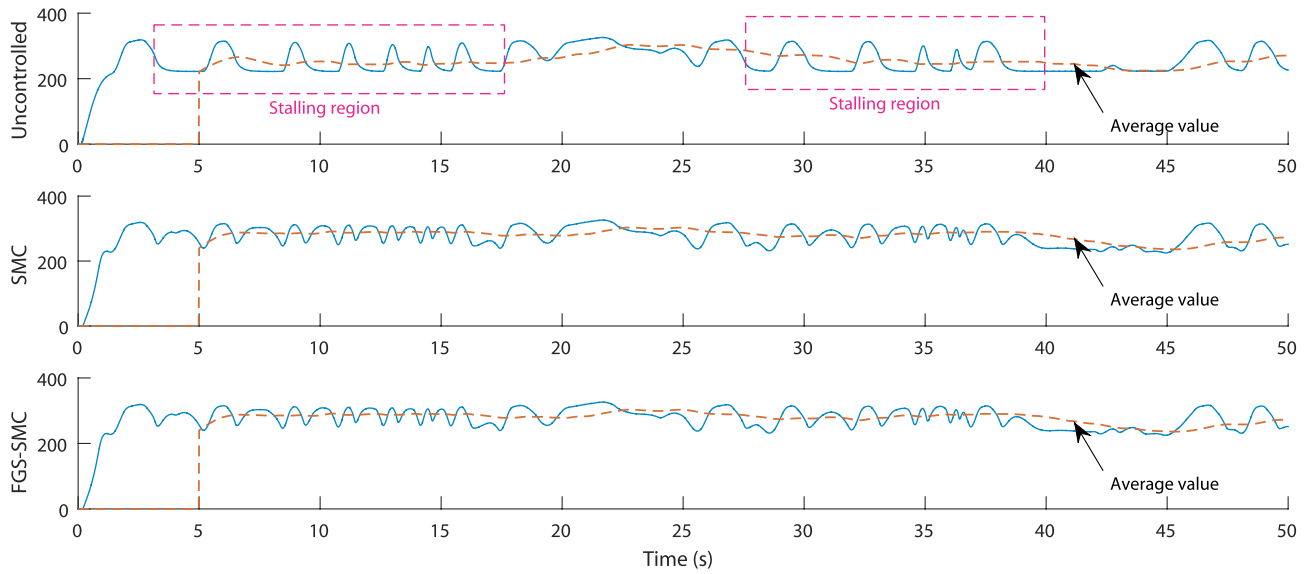


FIGURE 24. Produced torques with SMC and FGS-SMC rotational speed control.

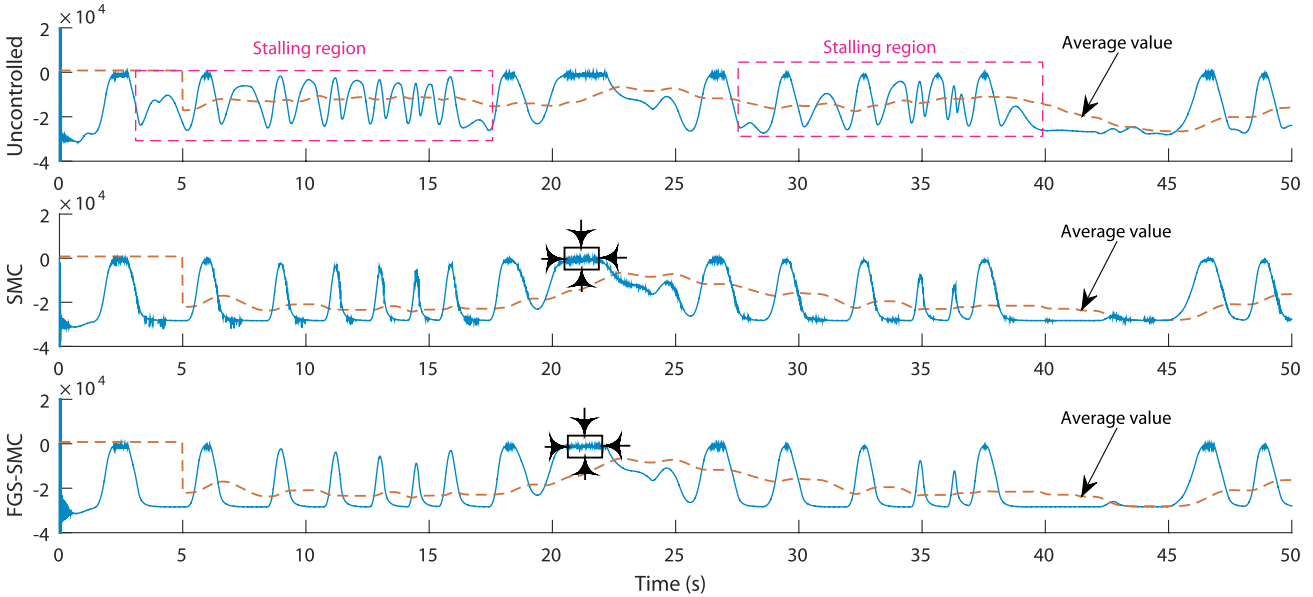


FIGURE 25. Generated powers with SMC and FGS-SMC rotational speed control.

The obtained rotational speed in the uncontrolled case and controlled cases are shown in Figure 22.

It can be noticed that two major stalling regions occur and that the rotational speed in the uncontrolled case at peak waves is low which will cause a peak in the flow coefficient and provoke the stalling behavior. However, in both controlled cases, the proposed control schemes help accelerate the speed to avoid the stalling behavior.

The resulting flow coefficients relative to the obtained rotational speeds in all three cases are presented in Figure 23.

In Figure 23 one may notice that in the stalling regions both controlled cases the flow coefficients are almost equal to the threshold value which is 0.3, contrary to the uncontrolled case where the flow coefficient exceeds it.

The obtained flow coefficients lead to the produced torques of Figure 24. The plots show that in the uncontrolled case the torque is affected with the stalling phenomenon that decreases its average value but both controlled cases have evaded the stalling phenomenon which helped produce more stable and higher torques in terms of average value.

Figure 25 shows the powers generated by the OWC in the three cases. As the uncontrolled case suffers from the stalling behavior, the power generated has been low especially in the stalling regions. However, both controlled cases have high generated power thanks to the proposed rotational speed strategy.

Also, one may notice that the power provided by the FGS-SMC is smoother than that of the SMC case. For a

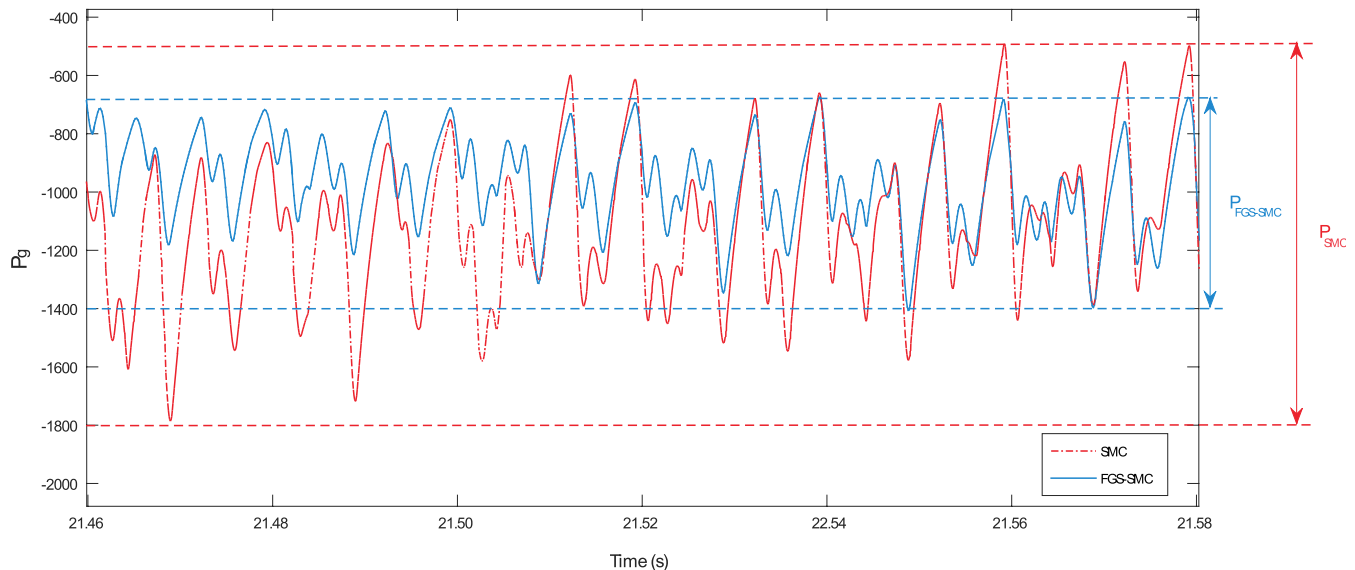


FIGURE 26. Zoom-in the generated powers with SMC and FGS-SMC rotational speed control.

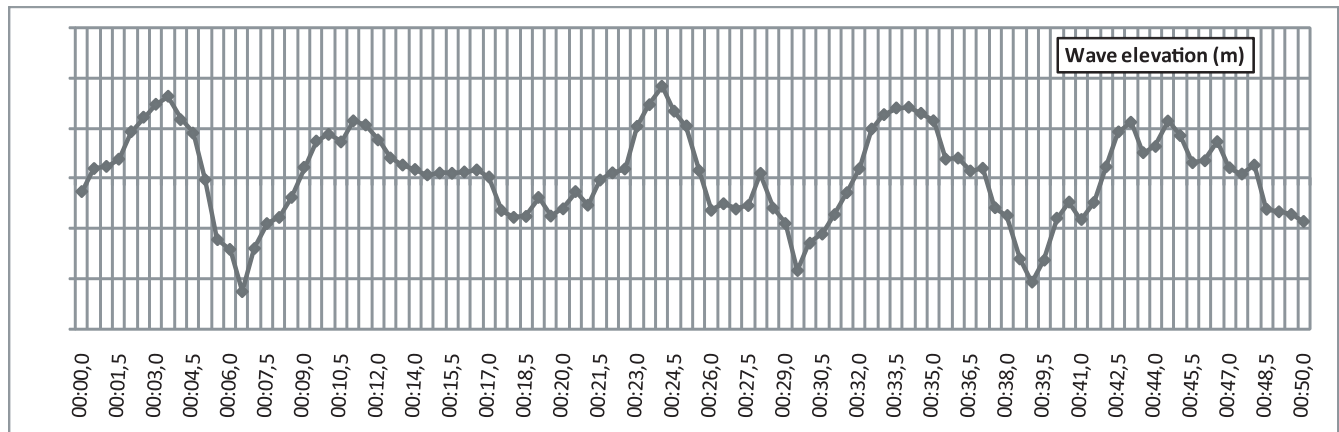


FIGURE 27. Wave elevation measured at Mutriku on May 12, 2014 at 06:00 am.

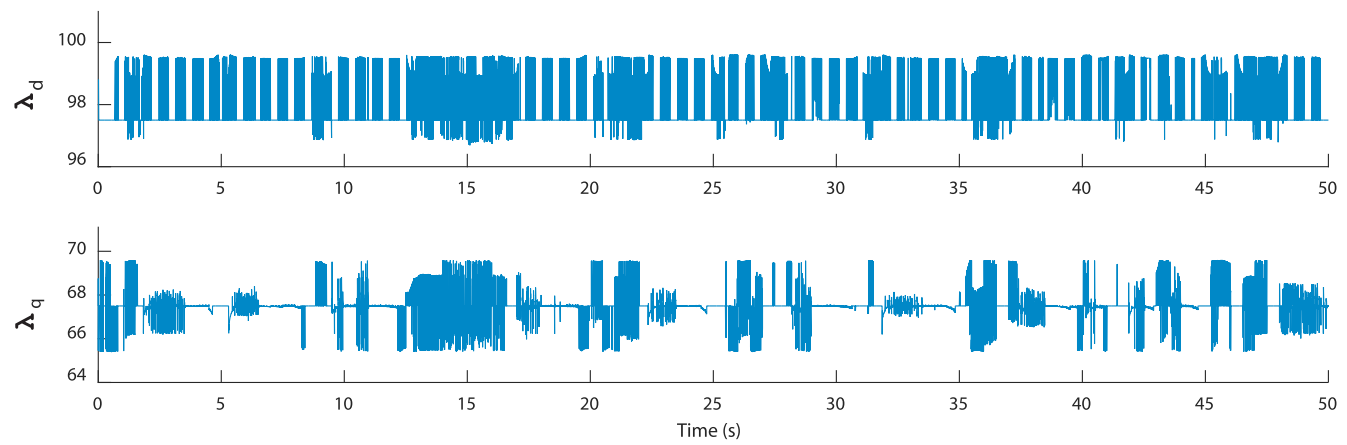


FIGURE 28. Time histories of control gains λ_d and λ_q .

better comparison both generated powers were overlapped and a zoom-in has been done into the same section at the peak wave of 21.5s as shown in Figure 25. Figure 26 shows that the FGS-SMC was able to improve the quality

of the generated power by reducing the fluctuations caused by the chattering phenomenon compared to the SMC. In fact the generated power with FGS-SMC is 46% less fluctuated.

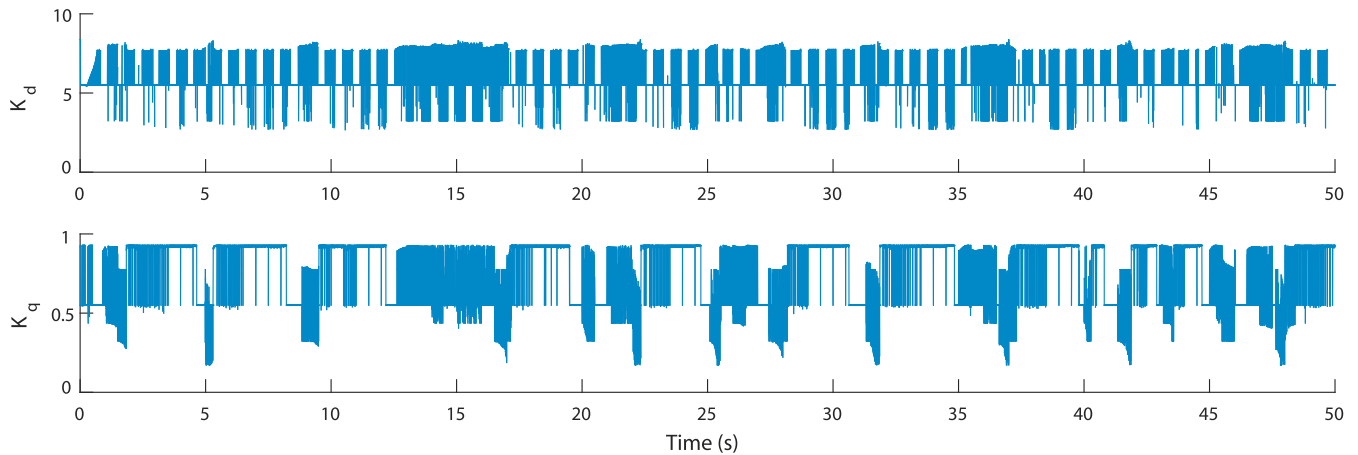


FIGURE 29. Time histories of control gains K_d and K_q .

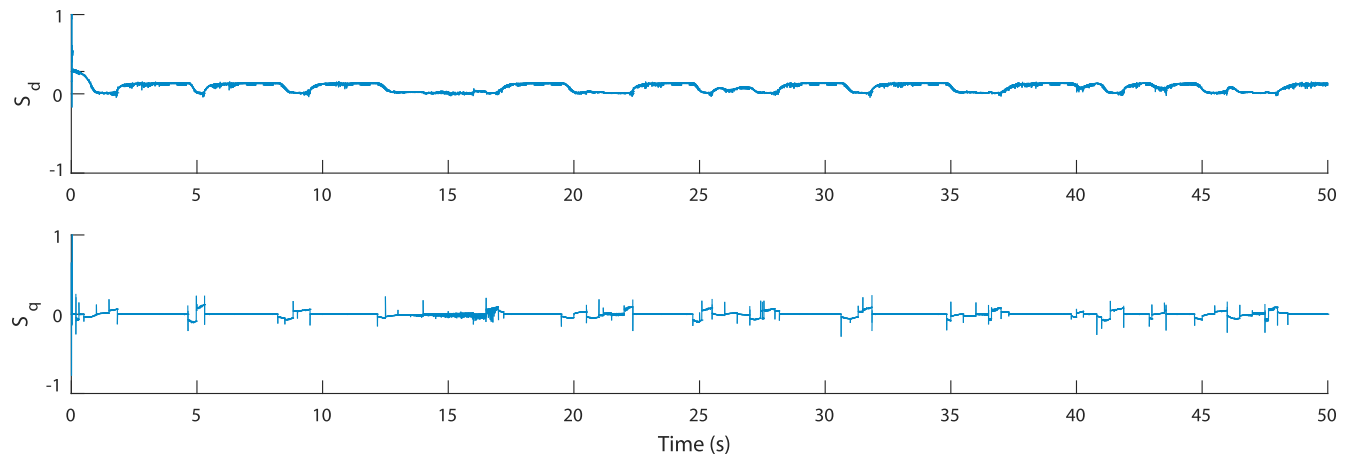


FIGURE 30. Time histories of the sliding variables S_d and S_q using SMC.

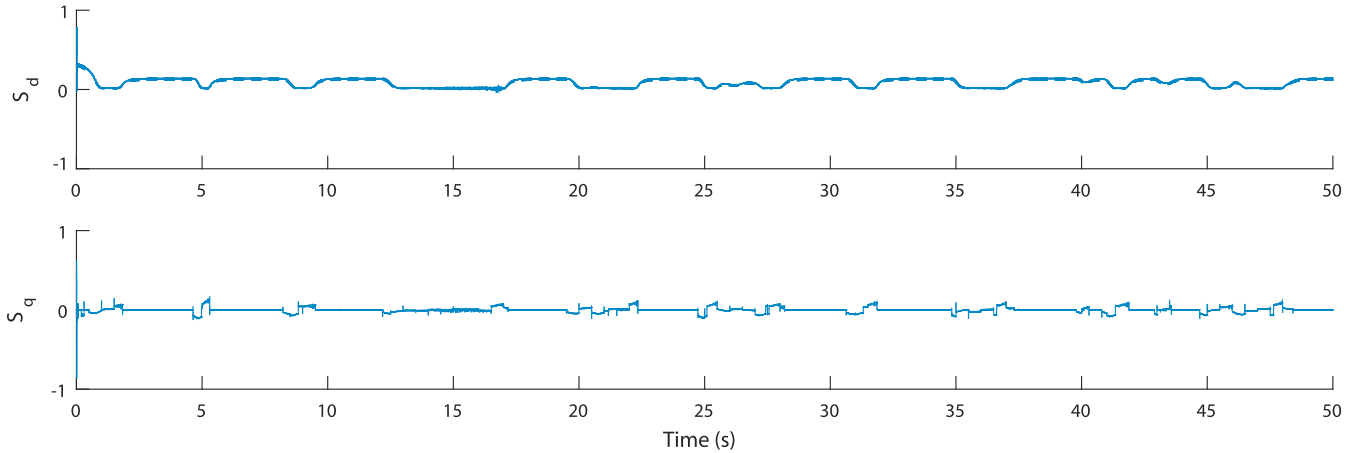


FIGURE 31. Time histories of the sliding variables S_d and S_q using FGS-SMC.

It is to be noted that the power to be injected into the grid would be passing through a filter to further reduce the fluctuations. A simple L-filter or LCL-filter is usually adopted to reduce the Total Harmonic Distortion (THD) of the utility current [64]. To meet the grid code requirements, the LCL-filter is predominant in reducing the utility current harmonics.

B. CASE STUDY USING REAL MEASURED WAVES

To further validate the results of the rotational speed control another study case considering real measured waves has been carried out. The wave data series were obtained from measurements of an Acoustic Doppler Current Profiler (ADCP) installed at Mutriku. These measurements are in the form

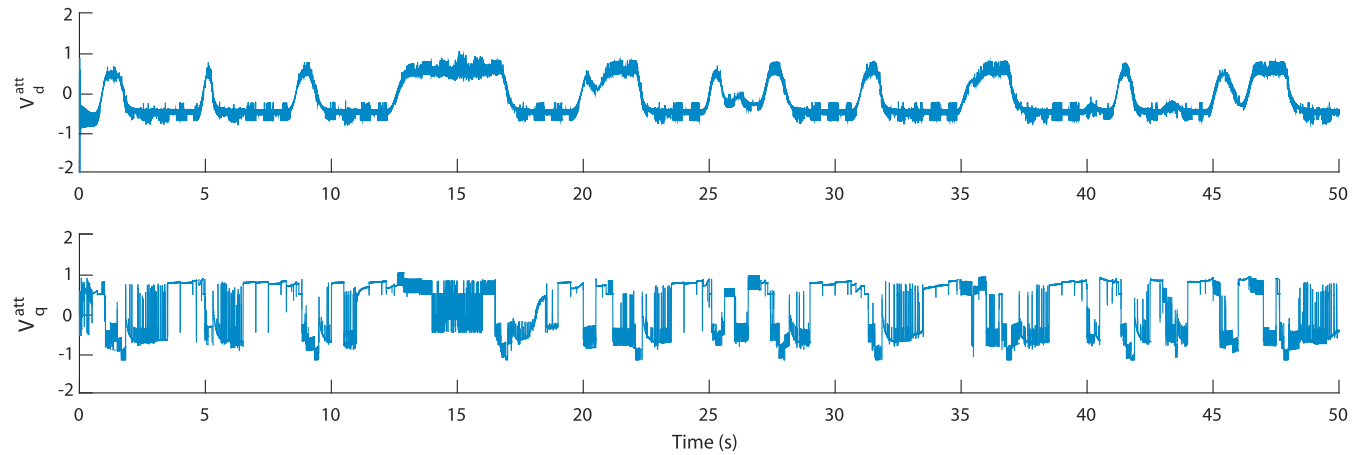


FIGURE 32. Switching detail of the generated attractive control voltages using SMC.

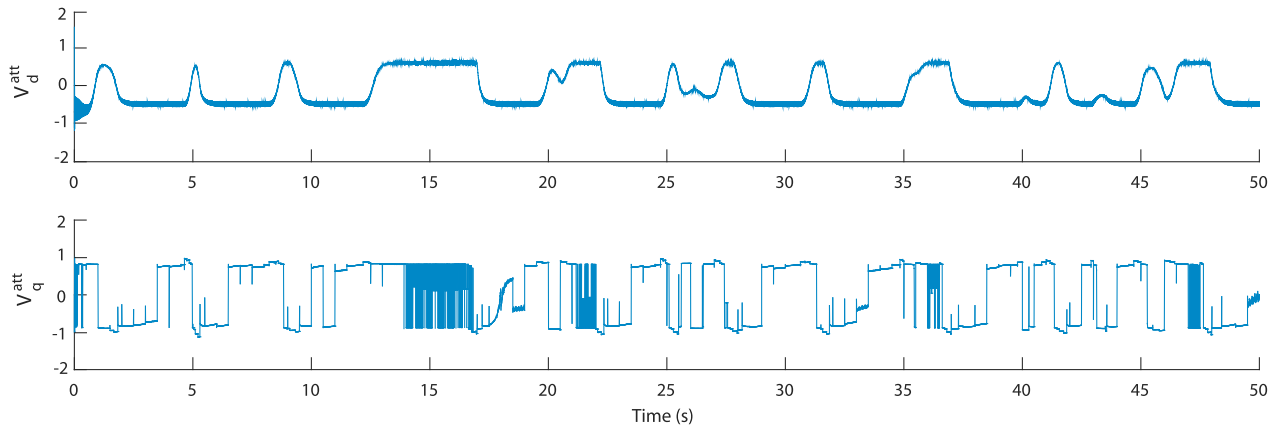


FIGURE 33. Switching detail of the generated attractive control voltages using FGS-SMC.

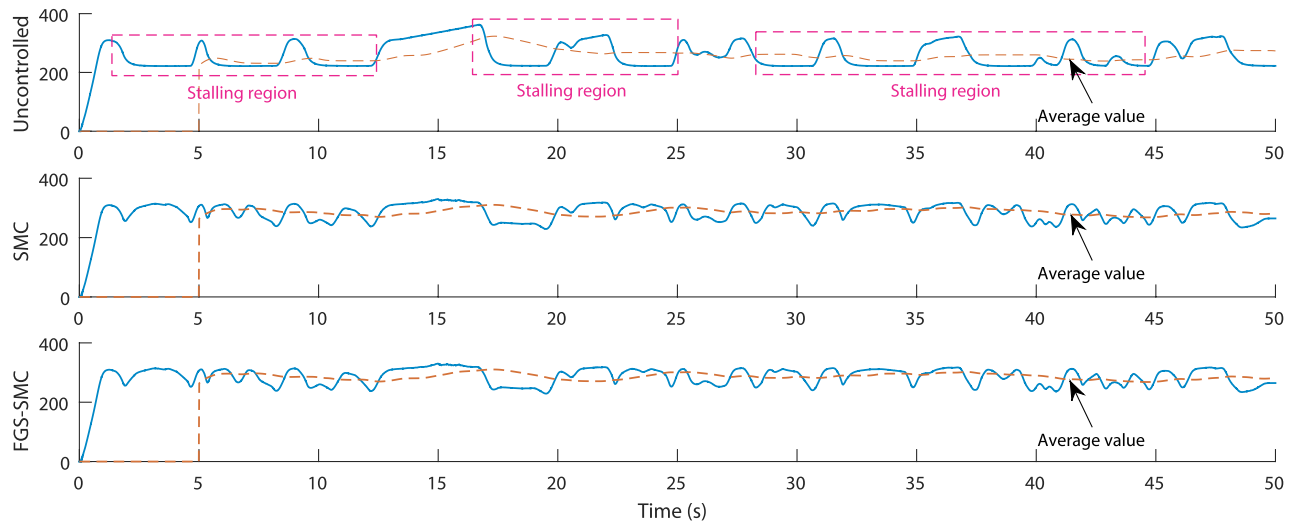


FIGURE 34. Rotational speeds with SMC and FGS-SMC rotational speed control.

of data series with a sampling period of 0.5s taken over 20 minutes every two hours during May 12, 2014 [18].

The considered wave input from that day is shown in Figure 27.

The obtained FGS-SMC varying control gains are illustrated in Figures 28 and 29.

The evolution of the sliding variables S_d and S_q with both SMC and FGS-SMC are presented in Figures 30 and 31.

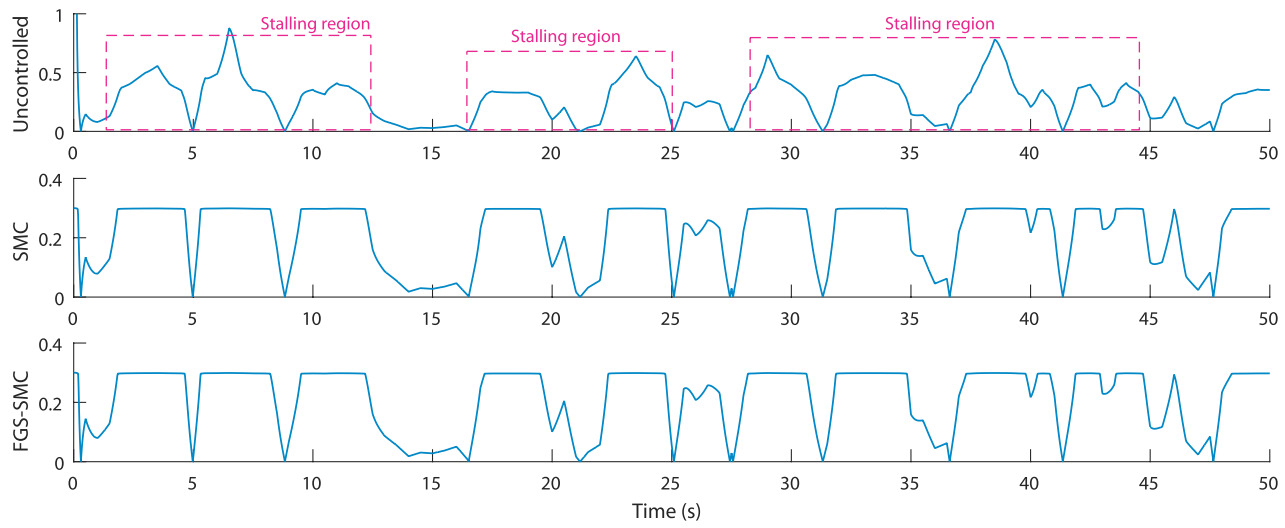


FIGURE 35. Flow coefficients with SMC and FGS-SMC rotational speed control.

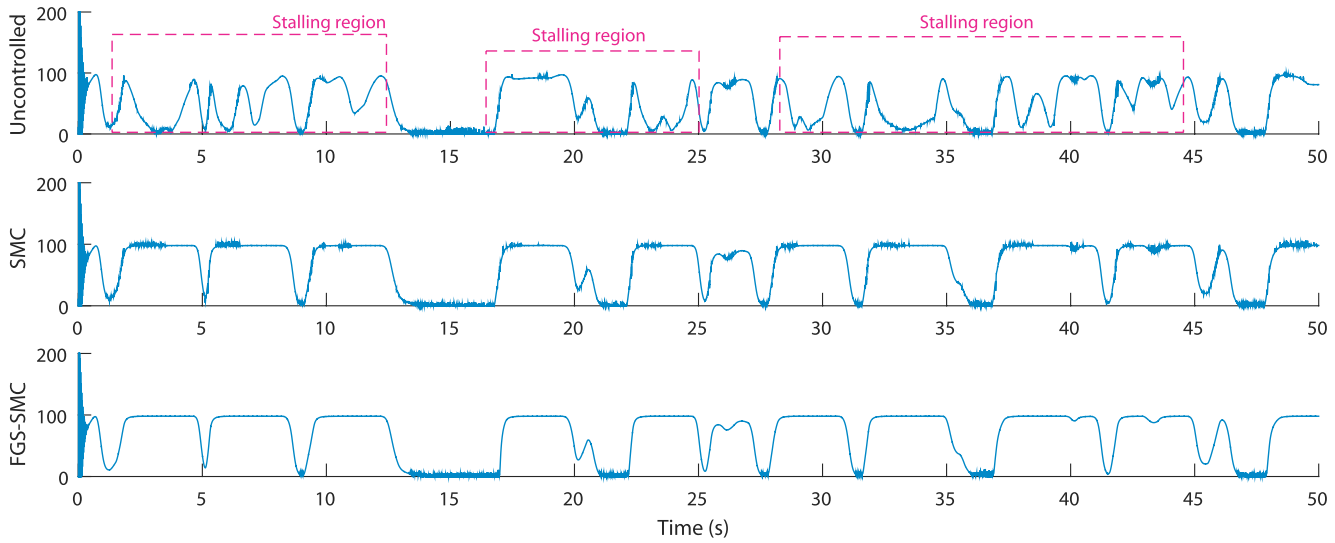


FIGURE 36. Produced torques with SMC and FGS-SMC rotational speed control.

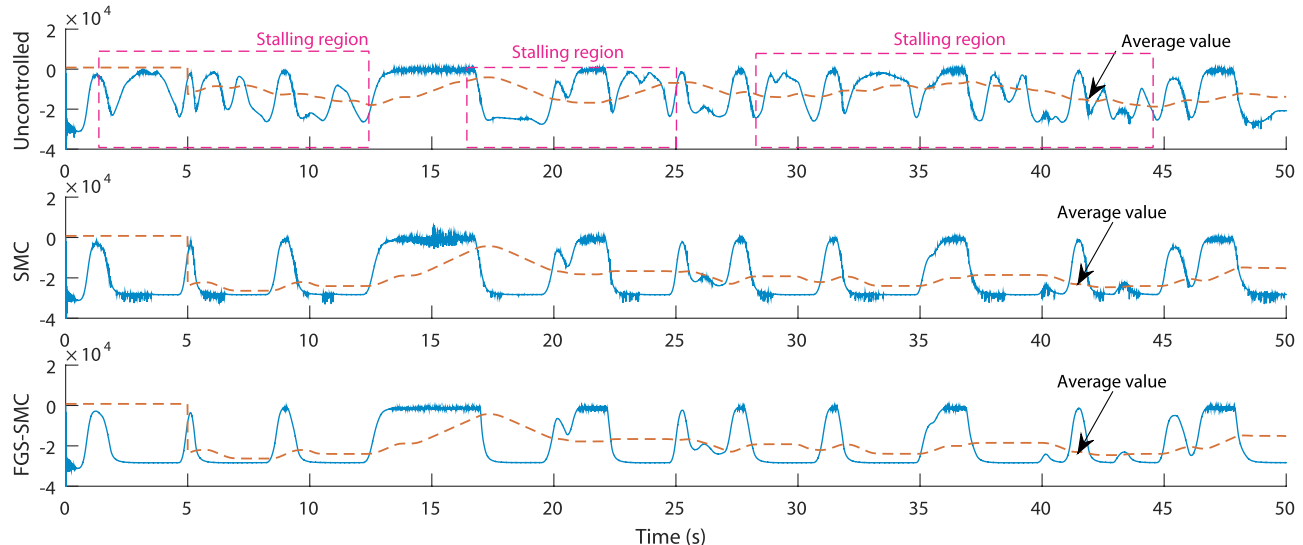


FIGURE 37. Generated powers with SMC and FGS-SMC rotational speed control.

The sliding variables are smoother and less chattering occurs with the FGS-SMC.

The obtained attractive control voltages are illustrated in Figures 32 and 33.

From the obtained rotational speeds depicted in Figure 34, three stalling regions are noticed. In these regions, the proposed controls tend to increase the speed whereas in the uncontrolled case it remains low.

Consequently, the obtained flow coefficients are regulated to 0.3 with the SMC and FGS-SMC control unlike the uncontrolled case where it exceeds it as shown in Figure 35.

The effect of regulating the flow coefficient is observed on the outputs which are the produced torques in Figure 36 and the generated powers in Figure 37. These outputs are stable and higher in terms of average value within all three stalling regions compared to the uncontrolled OWC, however, with the FGS-SMC control, we get smoother and less fluctuated results compared to the SMC control.

V. CONCLUSION

In this article, OWC system has been modeled and controlled. A Sliding Mode rotational speed control strategy was implemented to deal with the stalling behavior of the Wells turbine which restricts the generated power. The proposed SMC-based rotational speed control effectively governs the back-to-back converter to regulate the rotational speed of the turbo-generator shaft hence evade the stalling behavior.

To enhance the performance of the SMC-based rotational speed control the Fuzzy Gain Scheduling methodology has been proposed and implemented that adaptively varies the gains of the controller via designed fuzzy logic supervisors.

To assess the goodness of the suggested control strategies, irregular waves and real measured waves have been used for the study. The results demonstrate that the suggested control scheme successfully avoids the stalling behavior by accelerating and decelerating the shaft's rotational speed allowing the system to harness the maximum power from the incoming waves. Furthermore, the suggested control design FGS-SMC shows a superior performance against the fixed gain SMC method by reducing the chattering phenomenon. In fact, the FGS-SMC-based rotational speed control scheme offers 14.52% power generation whereas, the fixed-gains SMC-based rotational speed control scheme offers only 10.08% power generation improvement. Moreover, the FGS-SMC offers up to 45% less fluctuations.

REFERENCES

- [1] IPCC. (Oct. 8, 2018). *Special Report on Global Warming of 1.5°C (SR15)*. Accessed: Oct. 26, 2019. [Online]. Available: <https://www.ipcc.ch/sr15/>
- [2] IPCC. (Aug. 9, 2019). *Special Report on Climate Change, Desertification, Land Degradation, Sustainable Land Management, Food Security, and Greenhouse Gas Fluxes in Terrestrial Ecosystems (SRCCCL)*. Accessed: Oct. 26, 2019. [Online]. Available: <https://www.ipcc.ch/report/srcccl/>
- [3] IPCC. (Sep. 25, 2019). *Special Report on the Ocean and Cryosphere in a Changing Climate (SROCC)*. Accessed: Oct. 26, 2019. [Online]. Available: <https://www.ipcc.ch/srocc/home/>
- [4] Ocean Energy Forum. (Nov. 2016). *Ocean Energy Strategic Roadmap 2016, Building Ocean Energy for Europe*. Accessed: Oct. 26, 2019. [Online]. Available: <https://webgate.ec.europa.eu/maritimeforum/>
- [5] M. Alamir, M. Fiacchini, S. B. Chabane, S. Bacha, and T. Kovaltchouk, "Active power control under grid code constraints for a tidal farm," in *Proc. 11th Int. Conf. Ecological Vehicles Renew. Energies (EVER)*, Monte Carlo, Monaco, Apr. 2016, pp. 1–7.
- [6] D. Magagna and A. Uihlein, "2014 JRC Ocean Energy Status Report," Eur. Commission, Brussels, Belgium, Tech. Rep. OPOCE LD-NA-26983-EN-N, 2015.
- [7] A. Maria-Arenas, A. J. Garrido, E. Rusu, and I. Garrido, "Control strategies applied to wave energy converters: State of the art," *Energies*, vol. 12, no. 16, p. 3115, Aug. 2019.
- [8] V. Stratigaki, "WECANet: The first open pan-European network for marine renewable energy with a focus on wave energy-COST action CA17105," *Water*, vol. 11, no. 6, p. 1249, Jun. 2019.
- [9] L. Rusu and F. Onea, "Assessment of the performances of various wave energy converters along the European continental coasts," *Energy*, vol. 82, pp. 889–904, Mar. 2015.
- [10] *The European Marine Energy Center LTD*. Accessed: Oct. 26, 2019. [Online]. Available: <http://www.emec.org.uk/>
- [11] Y. Torre-Enciso, I. Ortubia, L. I. López de Aguilera, and J. Marqués, "Mutriku Wave Power Plant: From the thinking out to the reality," in *Proc. 8th Eur. Wave Tidal Energy Conf.*, Uppsala, Sweden, Sep. 2009, pp. 319–329.
- [12] W. K. Tease, J. Lees, and A. Hall, "Advances in oscillating water column air turbine development," in *Proc. 7th Eur. Wave Tidal Energy Conf.*, Porto, Portugal, Sep. 2007, pp. 1–9.
- [13] A. A. D. Carrelhas, L. M. C. Gato, J. C. C. Henriques, A. F. O. Falcão, and J. Varandas, "Test results of a 30 kW self-rectifying biradial air turbine-generator prototype," *Renew. Sustain. Energy Rev.*, vol. 109, pp. 187–198, Jul. 2019.
- [14] A. Arias, P. Izquierdo, P. Yañez, J. A. Vilán, and A. Segade, and E. Casarejos, *Design, Manufacturing and Set-Up Tests of a Wave Energy Converter Prototype in the Context of the European Project LIFE-Demowave*. Barcelona, Spain: SARTI, 2018.
- [15] A. F. D. O. Falcão and P. A. P. Justino, "OWC wave energy devices with air flow control," *Ocean Eng.*, vol. 26, no. 12, pp. 1275–1295, Dec. 1999.
- [16] M. Amundarain, M. Alberdi, A. J. Garrido, and I. Garrido, "Modeling and simulation of wave energy generation plants: Output power control," *IEEE Trans. Ind. Electron.*, vol. 58, no. 1, pp. 105–117, Jan. 2011.
- [17] S. K. Mishra, S. Purwar, and N. Kishor, "Air flow control of OWC wave power plants using FOPIID controller," in *Proc. IEEE Conf. Control Appl. (CCA)*, Sydney, NSW, Australia, Sep. 2015, pp. 1516–1521.
- [18] F. M'zoughi, S. Bouallègue, A. J. Garrido, I. Garrido, and M. Ayadi, "Stalling-free control strategies for oscillating-water-column-based wave power generation plants," *IEEE Trans. Energy Convers.*, vol. 33, no. 1, pp. 209–222, Mar. 2018.
- [19] F. M'zoughi, S. Bouallègue, A. J. Garrido, I. Garrido, and M. Ayadi, "Water cycle algorithm-based airflow control for an oscillating water column-based wave generation power plant," *Proc. Inst. Mech. Eng. I, J. Syst. Control Eng.*, vol. 234, no. 1, pp. 118–133, 2020.
- [20] Z. Yu, N. Jiang, and Y. You, "Load control method and its realization on an OWC wave power converter," in *OMAE*, vol. 1. New York, NY, USA: ASME, 1994.
- [21] P. A. P. Justino and A. F. de O. Falcão, "Rotational speed control of an OWC wave power plant," *J. Offshore Mech. Arctic Eng.*, vol. 121, no. 2, pp. 65–70, May 1999.
- [22] A. F. O. Falcão, J. C. C. Henriques, and L. M. C. Gato, "Rotational speed control and electrical rated power of an oscillating-water-column wave energy converter," *Energy*, vol. 120, pp. 253–261, Feb. 2017.
- [23] M. Amundarain, M. Alberdi, A. J. Garrido, and I. Garrido, "Neural rotational speed control for wave energy converters," *Int. J. Control.*, vol. 84, no. 2, pp. 293–309, Feb. 2011.
- [24] J. Lekube, A. J. Garrido, and I. Garrido, "Rotational speed optimization in oscillating water column wave power plants based on maximum power point tracking," *IEEE Trans. Autom. Sci. Eng.*, vol. 14, no. 2, pp. 681–691, Apr. 2017.
- [25] S. K. Mishra, S. Purwar, and N. Kishor, "An optimal and non-linear speed control of oscillating water column wave energy plant with wells turbine and DFIG," *Int. J. Renew. Energy Res.*, vol. 6, no. 3, pp. 995–1006, 2016.
- [26] S. Mishra, S. Purwar, and N. Kishor, "Maximizing output power in oscillating water column wave power plants: An optimization based MPPT algorithm," *Technologies*, vol. 6, no. 1, p. 15, Jan. 2018.
- [27] S. K. Mishra, S. Purwar, and N. Kishor, "Event-triggered nonlinear control of OWC ocean wave energy plant," *IEEE Trans. Sustain. Energy*, vol. 9, no. 4, pp. 1750–1760, Oct. 2018.

- [28] S. Raghunathan, "Performance of the Wells self-rectifying turbine," *Aeronaut. J.*, vol. 89, no. 890, pp. 37–369, 1985.
- [29] S. Raghunathan, "The wells air turbine for wave energy conversion," *Progr. Aerosp. Sci.*, vol. 31, no. 4, pp. 335–386, Jan. 1995.
- [30] J. P. Le Roux, "An extension of the airy theory for linear waves into shallow water," *Coastal Eng.*, vol. 55, no. 4, pp. 295–301, Apr. 2008.
- [31] A. J. Garrido, E. Otaola, I. Garrido, J. Lekube, F. J. Maseda, P. Liria, and J. Mader, "Mathematical modeling of oscillating water columns wave-structure interaction in ocean energy plants," *Math. Problems Eng.*, vol. 2015, pp. 1–11, Nov. 2015.
- [32] A. J. Garrido, I. Garrido, M. Amundarain, M. Alberdi, and M. De la Sen, "Sliding-mode control of wave power generation plants," *IEEE Trans. Ind. Appl.*, vol. 48, no. 6, pp. 2372–2381, Nov. 2012.
- [33] A. F. D. O. Falcão and R. J. A. Rodrigues, "Stochastic modelling of OWC wave power plant performance," *Appl. Ocean Res.*, vol. 24, no. 2, pp. 59–71, Apr. 2002.
- [34] W. Sheng, H. Li, and J. Murphy, "An improved method for energy and resource assessment of waves in finite water depths," *Energies*, vol. 10, no. 8, p. 1188, Aug. 2017.
- [35] T. Setoguchi and M. Takao, "Current status of self rectifying air turbines for wave energy conversion," *Energy Convers. Manage.*, vol. 47, nos. 15–16, pp. 2382–2396, Sep. 2006.
- [36] M. Alberdi, M. Amundarain, A. J. Garrido, I. Garrido, O. Casquero, and M. De la Sen, "Complementary control of oscillating water column-based wave energy conversion plants to improve the instantaneous power output," *IEEE Trans. Energy Convers.*, vol. 26, no. 4, pp. 1021–1032, Dec. 2011.
- [37] P. Ledesma and J. Usaola, "Doubly fed induction generator model for transient stability analysis," *IEEE Trans. Energy Convers.*, vol. 20, no. 2, pp. 388–397, Jun. 2005.
- [38] Z. Chen, J. M. Guerrero, and F. Blaabjerg, "A review of the state of the art of power electronics for wind turbines," *IEEE Trans. Power Electron.*, vol. 24, no. 8, pp. 1859–1875, Aug. 2009.
- [39] J. Fletcher and J. Yang, *Introduction to the Doubly-Fed Induction Generator for Wind Power Applications*. Rijeka, Croatia: InTech, 2010.
- [40] Y. Lei, A. Mullane, G. Lightbody, and R. Yacamini, "Modeling of the wind turbine with a doubly fed induction generator for grid integration studies," *IEEE Trans. Energy Convers.*, vol. 21, no. 1, pp. 257–264, Mar. 2006.
- [41] R. Pena, J. C. Clare, and G. M. Asher, "Doubly fed induction generator using back-to-back PWM converters and its application to variable-speed wind-energy generation," *IEE Proc. Electr. Power Appl.*, vol. 143, no. 3, pp. 231–241, May 1996.
- [42] D. Zhou and F. Blaabjerg, "Bandwidth oriented proportional-integral controller design for back-to-back power converters in DFIG wind turbine system," *IET Renew. Power Gener.*, vol. 11, no. 7, pp. 941–951, Jun. 2017.
- [43] S. Ebrahimkhani, "Robust fractional order sliding mode control of doubly-fed induction generator (DFIG)-based wind turbines," *ISA Trans.*, vol. 63, pp. 343–354, Jul. 2016.
- [44] C. A. Evangelista, A. Pisano, P. Puleston, and E. Usai, "Receding horizon adaptive second-order sliding mode control for doubly-fed induction generator based wind turbine," *IEEE Trans. Control Syst. Technol.*, vol. 25, no. 1, pp. 73–84, Jan. 2017.
- [45] N. Ullah, M. A. Ali, A. Ibeas, and J. Herrera, "Adaptive fractional order terminal sliding mode control of a doubly fed induction generator-based wind energy system," *IEEE Access*, vol. 5, pp. 21368–21381, 2017.
- [46] F. M'zoughi, A. J. Garrido, I. Garrido, S. Bouallegue, and M. Ayadi, "Sliding mode rotational speed control of an oscillating water column-based wave generation power plants," in *Proc. Int. Symp. Power Electron., Electr. Drives, Autom. Motion (SPEEDAM)*, Amalfi, Italy, Jun. 2018, pp. 1263–1270.
- [47] V. I. Utkin, "Sliding mode control design principles and applications to electric drives," *IEEE Trans. Ind. Electron.*, vol. 40, no. 1, pp. 23–36, Feb. 1993.
- [48] J.-J.-E. Slotine, "Sliding controller design for non-linear systems," *Int. J. Control.*, vol. 40, no. 2, pp. 421–434, 1984.
- [49] M. W. Naouar, E. Monmasson, A. A. Naassani, and I. Slama-Belkhodja, "FPGA-based dynamic reconfiguration of sliding mode current controllers for synchronous machines," *IEEE Trans. Ind. Informat.*, vol. 9, no. 3, pp. 1262–1271, Aug. 2013.
- [50] C.-K. Lin, "Nonsingular terminal sliding mode control of robot manipulators using fuzzy wavelet networks," *IEEE Trans. Fuzzy Syst.*, vol. 14, no. 6, pp. 849–859, Dec. 2006.
- [51] Y. Yang, "A time-specified nonsingular terminal sliding mode control approach for trajectory tracking of robotic airships," *Nonlinear Dyn.*, vol. 92, no. 3, pp. 1359–1367, Feb. 2018.
- [52] N. Luo, R. Villamizar, J. Vehi, J. Rodellar, and V. Manosa, "Sliding mode control of structures with uncertain coupled subsystems and actuator dynamics," in *Proc. Eur. Control Conf. (ECC)*, Cambridge, U.K., Sep. 2003, pp. 927–932.
- [53] A. Ibeas, "Superstability of linear switched systems," *Int. J. Syst. Sci.*, vol. 45, no. 11, pp. 2402–2410, Feb. 2013.
- [54] M. Niezabitowski, "On the sequences realizing perron and Lyapunov exponents of discrete linear time-varying systems," *Math. Problems Eng.*, vol. 2016, pp. 1–7, Nov. 2016, doi: [10.1155/2016/1487824](https://doi.org/10.1155/2016/1487824).
- [55] Z.-Y. Zhao, M. Tomizuka, and S. Isaka, "Fuzzy gain scheduling of PID controllers," *IEEE Trans. Syst., Man, Cybern.*, vol. 23, no. 5, pp. 1392–1398, Sep./Oct. 1993.
- [56] M. Tursini, F. Parasiliti, and D. Zhang, "Real-time gain tuning of PI controllers for high-performance PMSM drives," *IEEE Trans. Ind. Appl.*, vol. 38, no. 4, pp. 1018–1026, Jul. 2002.
- [57] A. I. Dounis, P. Kofinas, C. Alafodimos, and D. Tseles, "Adaptive fuzzy gain scheduling PID controller for maximum power point tracking of photovoltaic system," *Renew. Energy*, vol. 60, pp. 202–214, Dec. 2013.
- [58] F. M'zoughi, S. Bouallegue, A. J. Garrido, I. Garrido, and M. Ayadi, "Fuzzy gain scheduled PI-based airflow control of an oscillating water column in wave power generation plants," *IEEE J. Ocean. Eng.*, vol. 44, no. 4, pp. 1058–1076, Oct. 2019.
- [59] L. Zhou, J. Zhang, J. Dou, and B. Wen, "A fuzzy adaptive backstepping control based on mass observer for trajectory tracking of a quadrotor UAV," *Int. J. Adapt. Control Signal Process.*, vol. 32, no. 12, pp. 1675–1693, Oct. 2018.
- [60] S. Dian, S. Hoang, M. Pu, J. Liu, and L. Chen, "Gain scheduling based backstepping control for motion balance adjusting of a power-line inspection robot," in *Proc. 35th Chin. Control Conf. (CCC)*, Chengdu, China, Jul. 2016, pp. 441–446.
- [61] Y. Yang and Y. Yan, "Attitude regulation for unmanned quadrotors using adaptive fuzzy gain-scheduling sliding mode control," *Aerospace Sci. Technol.*, vol. 54, pp. 208–217, Jul. 2016.
- [62] Y. Yang and Y. Yan, "Trajectory tracking for robotic airships using sliding mode control based on neural network approximation and fuzzy gain scheduling," *Proc. Inst. Mech. Eng. I, J. Syst. Control Eng.*, vol. 230, no. 2, pp. 184–196, Dec. 2015.
- [63] N. Ben, S. Bouallègue, and J. Haggege, "Fuzzy gains-scheduling of an integral sliding mode controller for a quadrotor unmanned aerial vehicle," *Int. J. Adv. Comput. Sci. Appl.*, vol. 9, no. 3, pp. 132–141, 2018.
- [64] M. Lisserre, F. Blaabjerg, and S. Hansen, "Design and control of an LCL-filter-based three-phase active rectifier," *IEEE Trans. Ind. Appl.*, vol. 41, no. 5, pp. 1281–1291, Sep. 2005.



FARES M'ZOUGHI was born in Amman, Jordan, in 1988. He received the Engineering degree in mechatronics from the National Engineering School of Carthage (ENICarthe), Carthage, Tunisia, in 2013, the master's degree in automatic control and signal processing from the National Engineering School of Tunis (ENIT), Tunis, Tunisia, in 2014, the Ph.D. degree in engineering control, automation and robotics from the University of the Basque Country (UPV/EHU), Bilbao, Spain, and the Ph.D. degree in electrical engineering from ENIT, in 2018, in a cotutelle program framework. He is currently a Postdoctoral Researcher with the Automatic Control Group (ACG), University of the Basque Country (UPV/EHU), Bilbao, Spain. His current research interests include renewable energy applications, mechatronics, adaptive control, intelligent control design, and applied control of dynamic systems, in particular, wave power generation plants.



IZASKUN GARRIDO (Senior Member, IEEE) was born in Bilbao, Spain, in 1967. She received the M.Sc. degree in applied mathematics from the University of the Basque Country (UPV/EHU), Spain, and the M.Sc. degree in numerical analysis and programming and the Ph.D. degree in finite elements from Dundee University, U.K., in 1999. She has held several positions at the Potsdam Institute for Climate Impact Research, Germany; Konrad-Zuse-Zentrum für Informationstechnik Berlin, Germany; and the University of Bergen, Norway. She has been an Invited Researcher with Stanford University, Stanford, CA, USA, and the Lawrence Livermore National Laboratory, Livermore, CA, USA. Since 2009, she has been the Vice Dean of research and international relations with UPV/EHU, a contracted Expert for the Research Executive Agency (REA, EC) and also acts as an Expert Evaluator for the Spanish National Evaluation Agency (ANEPE) and the EraNet projects. She is currently a Full Professor with the Department of Automatic Control and Systems Engineering. She has more than 100 publications, has supervised several Ph.D. theses. Her current main research interest includes numerical simulation and control applied to ocean power generation and fusion.



AITOR J. GARRIDO (Senior Member, IEEE) was born in Bilbao, Spain, in 1972. He received the M.Sc. degree in applied physics, the M.Sc. degree in electronic engineering, and the Ph.D. degree in control systems and automation from the University of the Basque Country (UPV/EHU), Bilbao, in 1999, 2001, and 2003, respectively. Since 2000, he has been holding several research and teaching positions with the Automatic Control and Systems Engineering Department, University of the Basque Country, where he is currently a Full Professor of control engineering and the Head of the Automatic Control Group (ACG). He has more than 100 articles published in the main international conferences of the area, book chapters, and JCR-indexed journals. He has participated in more than 30 National and European research projects, several of them as a Principal Researcher, and is an Evaluator of the Research Executive Agency for H2020 projects and the National Agency of Evaluation and Prospective (ANEPE). He has supervised several Ph.D. theses. His current research interests include the applied control of dynamic systems, in particular, the control of ocean energy, nuclear fusion, and biological systems. He has served as a Reviewer for a number of international indexed journals and conferences.



MANUEL DE LA SEN was born in Arrigorriaga, Bizkaia, Basque, Spain. He received the M.Sc. degree (Hons.) in applied physics (electronics and automation) and the Ph.D. degree (High Honors and Special Mention) in applied physics from the University of the Basque Country, Bilbao, Spain, in 1975 and 1979, respectively, and the degree of Docteur d'État-en-Sciences Physiques (specialité Automatique et Traitement du Signal, High Honors) from the University of Grenoble, Grenoble, France, in 1987. He was a Visiting Professor with the University of Grenoble, Grenoble, France; the University of Newcastle, Newcastle, Australia; and The Australian National University, Canberra, Australia. He is currently a Professor of systems engineering and automatic control with the University of the Basque Country, where he serves as the Head of the Institute of Research and Development of Processes. He has coauthored more than 800 articles in scientific journals and conference proceedings. His main research interest areas are discrete and sampled-data control systems, non-periodic and adaptive sampling, adaptive control, fixed point theory, positive systems, stability, models for ecology, epidemic models, time-delay systems, artificial intelligence tools for dynamic systems, and ordinary differential equations. He was formerly a member of the Editorial Board of the *Electrosoft Journal* (Mechanical and Computational Engineering Publications). He is currently an Associate Editor of the following journals: *Applied Mathematical Sciences*, *Nonlinear Analysis*, *Modelling and Control*, *Mathematics in Engineering, Science and Aerospace. The Transdisciplinary International Journal*, *Discrete Dynamics in Nature and Society*, *Nonlinear Studies. The International Journal*, and *Fixed Point Theory and Applications*.

• • •